

Subspace-Aware Sparse Autoencoders for Effective Mechanistic Interpretability

Seyed Arshan Dalili Mehrdad Mahdavi

The Pennsylvania State University
{sbd5760,mzm616}@psu.edu

Abstract

Sparse Autoencoders (SAEs) are widely used for mechanistic interpretability in large language models, yet their standard formulation assigns each latent feature a single decoder direction, implicitly assuming features to be one-dimensional. We show that this assumption is in fundamental tension with the multi-dimensional structure of model features, and that the tension provably induces feature splitting through two distinct mechanisms. *Geometrically*, reconstructing a feature of intrinsic dimension $d_i \geq 2$ to error ε with single-direction decoders forces a number of atoms that is exponential in d_i . From an end-to-end *optimization* perspective, this splitting is not merely possible but actively preferred. We prove that there exists a continuous path from the true d_i -dimensional basis to a strictly lower risk of the ℓ_1 -regularized SAE objective, whose descent directions drive any trained dictionary into exactly that exponential regime. A single coherent feature is therefore fragmented across many near-collinear latents, producing spurious multiplicity and obscuring the intrinsic geometry that interpretability requires. Motivated by this, we introduce *Subspace-Aware Sparse Autoencoders* (SASA), which replace single-vector decoders with learned decoder subspaces, enforce block sparsity via Top- s group gating, and adapt each group’s effective rank with a nuclear-norm regularizer. We then establish a converse to the SAE result such that once the block size satisfies $r \geq d_i$, a single group not only *can* represent the entire feature slice but *is* the global minimizer of the SASA objective—unique up to block index and orthogonal rotation—exactly inverting the instability that fragments vector dictionaries. This consolidation reduces feature recovery to principal subspace estimation, yielding sample complexity *polynomial* in d_i rather than exponential—a decisive advantage given that every training activation costs an LLM forward pass. Empirically, on GPT-2 and Mistral-7B, SASA reduces feature splitting and absorption, improves monosemanticity and interpretability, and matches or exceeds standard SAEs while training on roughly half the token budget. The code can be found at <https://github.com/arshandalili/sasa>.

1 Introduction

Mechanistic interpretability of Large Language Models (LLMs) aims to reveal how these models internally encode and manipulate knowledge, providing insights crucial for diagnosing behavior [Wang et al., 2022, Conmy et al., 2023], enhancing robustness [García-Carrasco et al., 2024, Winninger et al., 2025], and ensuring alignment [Arditi et al., 2024, Lee et al., 2024]. Recently, Sparse Autoencoders (SAEs) have become a prominent tool in the mechanistic interpretability of LLMs. Rooted in the Superposition Hypothesis [Elhage et al., 2022] and Linear Representation Hypothesis (LRH) [Alain and Bengio, 2018, Park et al., 2024], SAEs aim at making LLMs’ representation interpretable by disentangling the representation into a *sparse* set of directions in the ambient space. SAEs achieve this by learning a compressed, sparse representation of the model’s high-dimensional activations, effectively isolating a small set of active directions that capture the most salient features of the data. Each of the directions in the decoder often corresponds to a distinct, one-dimensional semantic feature, allowing for a more fine-grained, interpretable mapping between the model’s internal representations and specific concepts or patterns.

Nevertheless, interpreting LLM representations with SAEs remains challenging for both training and inference. From a training perspective, SAEs require large corpora of LLM activations (e.g., hidden states from specific layers and token positions). In practice, this often means billions of hidden states,



Figure 1: **Standard SAEs split a multi-dimensional feature across many near-collinear atoms, while SASA captures it as a single subspace.** We embed three ground-truth concept manifolds—a circle ($d_i = 2$), a sphere \mathbb{S}^2 ($d_i = 3$), and a helix ($d_i = 3$)—into an ambient space of dimension $d = 64$ (with 5% noise) and fit six dictionaries of width 256. *First column:* each manifold colored by its underlying concept value. *Next five columns:* standard vector-based SAEs (ReLU, TopK, BatchTopK, JumpReLU, Gated), in which every latent is tied to a single decoder direction. Each point is colored by the decoder atom most aligned with it. Under the vector-based assumption, the feature is *not* captured by one direction but is instead distributed across tens to hundreds of near-duplicate atoms, each explaining only a local slice of the manifold. Hence, interpreting the feature requires aggregating a whole cluster of latents rather than inspecting a single unit. *Last column:* SASA, which learns decoder *subspace* as the unit of representation. With the same total width, a single active group of effective rank d_i (one latent) covers the entire feature, recovering its intrinsic geometry rather than fragmenting it. For more elaboration and analysis

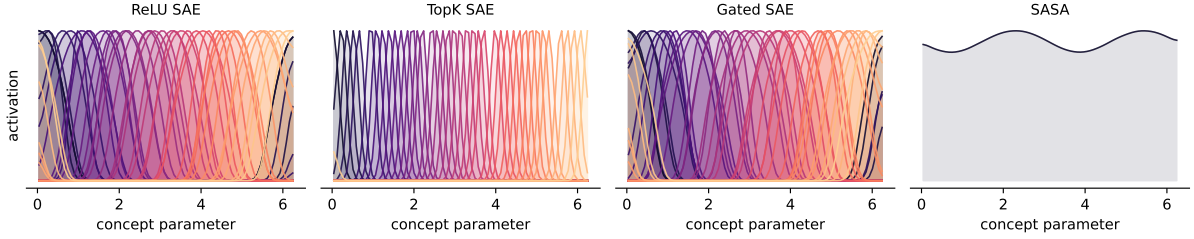
which limits scaling to large models. From an inference perspective, existing SAEs can learn *redundant* latents—multiple vectors corresponding to the same underlying feature—a phenomenon known as *feature splitting* [Bricken et al., 2023]. Feature splitting further makes interpretation challenging and fragmented, and, as we show in Section 6, results in worse sample complexity for learning the underlying features.

Intuitively, an SAE exhibits feature splitting when a single semantic feature is not captured by one decoder vector, but is instead distributed across many decoder directions. Each direction explains only a local “slice” of the factor, so interpretation requires aggregating a cluster of near-duplicate latents rather than inspecting a single unit (Figure 1). In Section 4 we formalize this intuition via a covering number and show that SAE loss actively moves toward such tiling solutions of the underlying feature subspace.

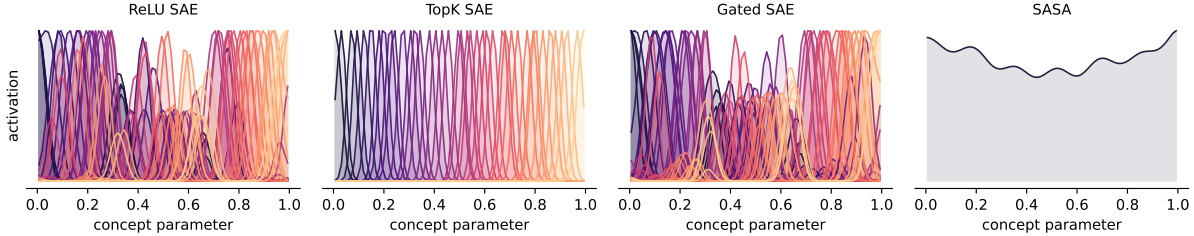
In parallel, recent empirical observations in LLM representations suggest an extension of the long-held LRH, named as Multi-dimensional LRH [Engels et al., 2025, Modell et al., 2025]. Unlike LRH, Multi-dimensional LRH suggests that features are not represented by a *vector* in the ambient space, but rather by *subspaces*. That said, features such as day, year, and colors exhibit circular representations. Building on these empirical findings, a natural question arises: if LLM features are structured as low-dimensional *subspaces* rather than single directions, what does this imply for SAEs, whose objective is to recover a *sparse set of vectors*? Collectively, these observations suggest a fundamental geometric incompatibility between the structure of features in modern LLM representations and the vector-level sparsity assumptions underlying standard SAEs, one that may manifest as the redundant and fragmented learned vectors commonly observed as feature splitting.

Contributions. We make the following contributions:

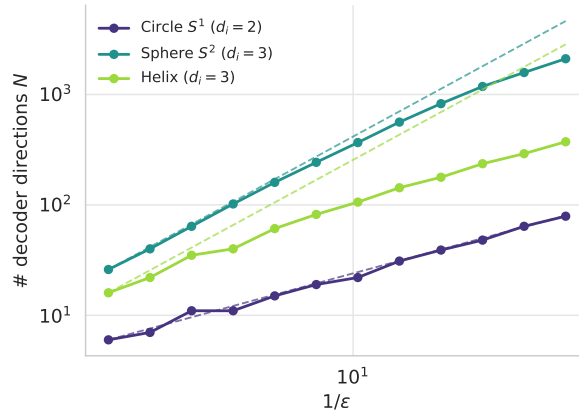
- We identify a geometric mismatch between the multi-dimensional feature structure suggested by the Multi-dimensional LRH and the vector-feature assumptions implicit in standard SAEs, and show how this mismatch can causally induce feature splitting.
- We formalize the notion of feature splitting for SAEs and give a principled criterion for when a



(a) Latent activation profiles for circle.



(b) Latent activation profiles for helix.



(c) Line-covering number.

Figure 2: **Standard SAEs fragment the manifold for a feature while SASA uses one broad group, and the cost of covering it with vectors grows with intrinsic dimension, as in Theorem 4.** (a,b) Activation of each latent along the concept parameter, for a circle and a helix. Vector-based SAEs (ReLU, TopK, Gated) tile the manifold with many narrow, overlapping tuning curves and no single latent represents the feature, whereas one SASA group responds broadly across the entire range. (c) Number of decoder directions N needed to cover a feature slice of intrinsic dimension d_i to error ε . The empirical count (solid) tracks the Theorem 4 lower bound (dashed), so the vector budget explodes as d_i grows and ε shrinks.

single multi-dimensional feature is fragmented across many learned vectors. We further show that, when features are inherently multi-dimensional and low reconstruction error is required, splitting is unavoidable across broad regimes. Importantly, we show that this is not merely a geometric necessity, but rather what the objective of SAE actively favors.

- We propose *Subspace-Aware Sparse Autoencoders (SASA)*, which incorporate multi-dimensional structure directly into the SAE objective through group sparsity with a rank-adaptive regularizer. By moving sparsity to the group level, it removes the structural pressure that splits multi-dimensional features, mitigating splitting and improving interpretability.
- We show that SASA improves sample complexity over standard SAE, which is a main bottleneck during training as each data point is an inference of an LLM.
- Finally, we validate these gains empirically on synthetic and real-world data and models.

Roadmap. The paper is organized as follows: Section 3 formalizes the multi-dimensional superposition hypothesis and reviews standard SAEs. In Section 4, we make feature splitting precise via a k -sparse covering criterion, whose worst case—the $k = 1$ line-covering regime—provably forces standard SAEs to allocate many decoder directions to achieve low reconstruction error. We then show that ℓ_1 sparsity actively drives a trained dictionary into exactly this regime. Motivated by the negative results of SAEs, Section 5 introduces SASA, which represents features with low-rank subspaces and enforces structured sparsity over these subspaces. We then show that SASA can both capture the feature and its minimizer actually reaches the top- d_i dimensional eigenspace of data. Section 6 then shows how this subspace-based view yields improved sample-complexity guarantees for recovering the underlying feature structure. Finally, Section 7 presents empirical results corroborating our theoretical findings and demonstrating the efficiency of SASA. Detailed proofs of the technical results, implementation details, and additional experimental evidence and evaluations are presented in the appendix.

2 Related Work

Mechanistic Interpretability. Mechanistic interpretability seeks mechanistic accounts of neural network behavior, typically validated via targeted interventions. Wang et al. [2022] demonstrated that complex behaviors can be decomposed into compact circuits that remain functional under controlled ablations and activation patching. Subsequent work has begun to automate this workflow, for example, by automatically identifying sparse, behavior-preserving subgraphs in the computational graph [Conmy et al., 2023]. Despite the progress made, Mechanistic Interpretability faces key challenges and questions, namely how to decompose networks into meaningful, causally-relevant components and how to rigorously validate mechanistic hypotheses to distinguish faithful explanations from misleading interpretability illusions [Sharkey et al., 2025].

LLM Representations. A central line of work in Deep Learning studies *representation hypotheses* that posit a simple geometric structure for semantic variables in activation space. Early work emphasized a largely one-dimensional view: many concepts should be recoverable as approximately linear directions [Harris, 1954], which motivates linear probing as an operational test of where information is encoded [Alain and Bengio, 2018, Park et al., 2024]. More recently, this perspective has been broadened into multi-dimensional hypotheses, where concepts may correspond to low-dimensional subspaces or more structured geometric objects (e.g., simplices) under an appropriate notion of contrast and inner product [Engels et al., 2025, Park et al., 2025]. These hypotheses matter for mechanistic interpretability because they define concrete geometric targets for measurement and causal testing: once a concept’s structure is specified, probes, interventions, and steering can be applied with respect to that structure rather than individual neurons. To date, much of the mechanistic interpretability literature has implicitly aligned with the one-dimensional version of these hypotheses, but the emerging multi-dimensional evidence motivates revisiting our tools and analyses in the setting where features occupy subspaces instead of single directions.

Modell et al. [2025] *conjectures* that feature splitting is a symptom of inherently multi-dimensional features: when a true feature occupies a low-dimensional subspace, standard vector SAEs are not proper *causal* mediators and instead approximate that subspace with multiple dictionary vectors [Engels et al., 2025, Bhalla et al., 2026]. Our analysis makes this conjecture precise, and our experiments confirm the underlying geometric assumption articulated by Michaud et al. [2025]. Also recently, Bhalla et al. [2026] formalize what it means for an SAE to capture a concept manifold and prove that an *idealized* sparse decoder over a sufficiently incoherent dictionary recovers the manifold subspace. Empirically, they show that trained SAEs do not reach this idealized decoder and instead settle into a fragmented regime they term *dilution*, in which a single manifold is distributed across many partially redundant atoms rather than a compact group. Yet they do not provide an analysis of why this phenomenon occurs, and the training objective drives SAEs toward fragmented solutions rather than toward the ideal decoder. We answer this question by proving that the ℓ_1 SAE objective actively rejects the subspace basis and descends toward this fragmented covering solution.

Superposition. The superposition hypothesis explains why neuron-level interpretations often fail: models can represent many sparse features in a limited activation space, producing polysemantic units and interference [Elhage et al., 2022]. This motivates dictionary learning methods that aim to recover a more feature-aligned basis than neurons. Sparse autoencoders (SAEs) are a widely used unsupervised approach in this line, learning sparse latents whose decoded directions reconstruct activations and often

admit semantic interpretations [Bricken et al., 2023]. Yet their training is challenging, as they usually require many hidden states from the LLM to train, motivating the search for more efficient, but less interpretable, methods [Leask et al., 2025].

Standard SAEs. Most SAE variants implement a vector dictionary: activations are reconstructed as sparse combinations of decoder directions, with sparsity enforced by mechanisms such as ReLU [Bricken et al., 2023], JumpReLU [Rajamanoharan et al., 2024b], gating [Rajamanoharan et al., 2024a], Top- k [Gao et al., 2020], BatchTopK [Bussmann et al., 2024], and Matryoshka [Bussmann et al., 2025]. Recent scaling analysis shows that when features have manifold structure, SAEs may allocate many vectors to cover a single manifold, resulting in far fewer distinct learned features than the model width would suggest [Michaud et al., 2025]. These limitations motivate moving beyond vector vectors toward subspace-level features, using structured sparsity and low-rank control to represent a single factor as a compact learned subspace rather than a cluster of directions [Yuan and Lin, 2006, Candès and Recht, 2009, Theodosis et al., 2022].

3 Problem Formulation and Preliminaries

Notation. We use bold-faced font to denote vectors and matrices, e.g., $\mathbf{x} \in \mathbb{R}^d$ and $\mathbf{X} \in \mathbb{R}^{a \times b}$. Furthermore, we use calligraphic notations to denote a set, e.g., \mathcal{X} . We let $[n] := \{1, 2, \dots, n\}$. For a vector $\mathbf{x} \in \mathbb{R}^d$, $[\mathbf{x}]_i \in \mathbb{R}$ is the i -th element of it, $\|\mathbf{x}\|_2$ denotes its Euclidean norm. For a matrix $\mathbf{X} \in \mathbb{R}^{d \times d}$, we let $\|\mathbf{X}\|_2$ be its spectral norm and $\text{tr}(\mathbf{X})$ denotes its trace. For a linear subspace $\mathcal{V} \subset \mathbb{R}^d$ with $\dim(\mathcal{V}) = d' < d$, let $\mathbf{V} \in \mathbb{R}^{d \times d'}$ be an orthonormal basis and $\mathbf{P}_{\mathcal{V}} = \mathbf{V}\mathbf{V}^\top$ be the orthogonal projector onto \mathcal{V} , and define the distance of a point \mathbf{x} from subspace \mathcal{V} as $\text{dist}(\mathbf{x}, \mathcal{V}) := \inf_{\mathbf{v} \in \mathcal{V}} \|\mathbf{x} - \mathbf{v}\|_2$. The unit sphere in \mathbb{R}^d is denoted by $\mathbb{S}^{d-1} := \{\mathbf{u} \in \mathbb{R}^d : \|\mathbf{u}\|_2 = 1\}$.

With the notation equipped, we now define our data generation process based on the multi-dimensional superposition hypothesis on LLM representations [Modell et al., 2025, Engels et al., 2025]. Appendix D provides empirical evidence that this feature structure arises intrinsically in representations learned by real-world LLMs, while Appendix E demonstrates that it can be recovered by SAEs.

Multi-dimensional superposition hypothesis. We model an activation $\mathbf{h} \in \mathbb{R}^d$ of an LLM at a fixed layer and token position (e.g., a residual stream vector or MLP) as a superposition of a small number of low-dimensional features. Let $\mathcal{I} = [m]$ index the features and each feature $i \in \mathcal{I}$ has a corresponding subspace $\mathcal{V}_i \subset \mathbb{R}^d$ with intrinsic dimension $1 \leq d_i \leq d$ and an orthonormal basis $\mathbf{V}_i \in \mathbb{R}^{d \times d_i}$. The following hypothesis models our generation process for \mathbf{h} .

Hypothesis 1 (Multi-dimensional Superposition Hypothesis). *There exist intrinsic dimensions $\{d_i \geq 1\}_{i=1}^m$, matrices $\{\mathbf{V}_i \in \mathbb{R}^{d \times d_i}\}_{i=1}^m$, feature coordinates $\{\mathbf{z}_i \in \mathbb{R}^{d_i}\}_{i=1}^m$, and noise $\boldsymbol{\xi} \in \mathbb{R}^d$, such that, for each $\mathbf{h} \in \mathbb{R}^d$, we have*

$$\mathbf{h} = \sum_{i=1}^m \mathbf{V}_i \mathbf{z}_i + \boldsymbol{\xi} \quad (1)$$

with the following holds:

1. (**Low-rank support**) $\dim(\mathbf{V}_i) = d_i$
2. (**Sparsity**) There exists $1 \leq s \ll m$ such that $|\{i : \mathbf{z}_i \neq \mathbf{0}\}| \leq s$.
3. (**Coherence**) There exists $0 \leq \mu \ll 1$ such that for all $i \neq j$, \mathbf{V}_i and \mathbf{V}_j are μ -coherent, meaning $|\mathbf{u}^\top \mathbf{v}| \leq \mu$ for all unit vectors $\mathbf{u} \in \text{col}(\mathbf{V}_i)$ and $\mathbf{v} \in \text{col}(\mathbf{V}_j)$. Furthermore, due to the orthonormality of the columns within each block \mathbf{V}_i , the sub-coherence, defined as the maximum coherence within each block, is zero. Assume the necessary condition for block recovery holds, i.e., $s < \frac{1}{2}(1 + \frac{1}{\mu})$ [Eldar et al., 2010].

We denote the resulting distribution over hidden states by \mathcal{D} , and assume access to i.i.d. samples $\mathcal{S} := \{\mathbf{h}_i\}_{i=1}^n$ with $\mathbf{h}_i \sim \mathcal{D}$. Hypothesis 1 raises two non-convex inference problems: (i) identifying the active set for an \mathbf{h} , i.e., $\{i : \mathbf{z}_i \neq \mathbf{0}\}$, and (ii) identifying basis \mathbf{V}_i for the active features' subspaces. A sparse autoencoder solves these two inference problems through its *encoder* and *decoder*. To analyze a single feature in isolation, we write $\mathcal{M}_i(t) := \{\mathbf{V}_i \mathbf{z}_i : \|\mathbf{V}_i \mathbf{z}_i\|_2 = t\}$ for the *noiseless single-feature slice* of feature i , i.e., the radius- t sphere inside the subspace \mathcal{V}_i (with \mathbf{V}_i orthonormal, equivalently $\{t\mathbf{u} : \mathbf{u} \in \mathbb{S}^{d-1} \cap \mathcal{V}_i\}$). The lower bounds and the recovery guarantees are stated over $\mathcal{M}_i(t)$.

Standard sparse autoencoders. A standard sparse autoencoder (SAE) with m latents is parameterized by an encoder $\mathbf{E} \in \mathbb{R}^{d \times m}$ and a decoder $\mathbf{D} \in \mathbb{R}^{d \times m}$. Define the latent activations as $a(\mathbf{h}) := \sigma(\mathbf{E}^\top \mathbf{h})$ (for simplicity, we drop biases). The SAE decoder associates each latent with a single direction $\mathbf{d}_j \in \mathbb{R}^d$, so that $\hat{\mathbf{h}} = \sum_j [a(\mathbf{h})]_j \mathbf{d}_j$. For analysis, we take the general objective form to be the standard reconstruction and ℓ_1 sparsity objective:

$$\min_{\mathbf{E}, \mathbf{D}} \sum_{i=1}^n \left[\|\mathbf{h}_i - \mathbf{D} a(\mathbf{h}_i)\|_2^2 + \lambda \|a(\mathbf{h}_i)\|_1 \right] \quad \text{s.t.} \quad \|\mathbf{d}_j\|_2 = 1 \quad \forall \mathbf{d}_j \in \mathbf{D}. \quad (2)$$

These models are popularly used to solve the inference problems raised by Hypothesis 1: identifying the active set is realized by $a(\mathbf{h})$, and identifying the basis \mathbf{V}_i is realized by \mathbf{D} . However, as we show in Section 4, this formulation fails to recover the correct \mathbf{V}_i s and instead learns many redundant, nearly collinear directions that fragment each multi-dimensional feature. Motivated by this, in Section 5 we propose a solution to alleviate this issue and in Section 6 we show that it leads to improved sample-complexity guarantees for recovering the underlying feature structure, thus significantly reducing the end-to-end training time.

4 On the Necessity of Subspace Learning

Standard SAEs assign each latent a single decoder direction, treating every semantic feature as one-dimensional. When a feature is inherently multi-dimensional and irreducible, this assumption carries two consequences that we make precise in this section. The first (Section 4.1) is purely geometric and states that any decoder restricted to co-activate at most $k < d_i$ directions per input feature must allocate a number of atoms that grows exponentially in $(d_i - k)/k$, causing splitting, and this count collapses to d_i only once k reaches d_i . The second—and perhaps the more important one—is that splitting is not merely a geometric possibility but the solution that the standard SAE objective actively prefers (Section 4.2). The true d_i -dimensional basis is unstable under the objective, and there exists a continuous path from it to a strictly lower population risk, while moving toward an overcomplete covering solution strictly decreases that risk. Together, these results give a causal and geometric account of feature splitting. The single-direction decoder assumption renders splitting both representationally necessary and dynamically preferred, which in turn motivates the subspace design of Section 5. We develop these two consequences in turn. We begin with the geometric one, asking how many decoder directions a standard dictionary must allocate to reconstruct every realization of a single multi-dimensional feature, a count that grows without bound as the demanded reconstruction error shrinks. All proofs are in Appendix A.1.

4.1 The subspace-covering phase transition

Fix feature $i \in \mathcal{I}$ with intrinsic dimension $d_i \geq 2$. On the noiseless single-feature slice $\mathcal{M}_i(t)$, i.e., $\mathbf{h} = \mathbf{V}_i \mathbf{z}_i \in \mathcal{V}_i$ with $\|\mathbf{h}\|_2 = t$, a decoder with co-activation budget k represents each input via the span of at most k of its N columns. We formalize the minimum N required for uniform ε -approximation. The exponent $(d_i - k)/k$ below decays in k and reaches zero at $k = d_i$, so a decoder allowed to co-activate $k \geq d_i$ atoms incurs no splitting and the bound bites precisely in the small-budget regime. As we show in Section 4.2, the standard SAE objective drives a trained dictionary into the extreme $k = 1$ (line-covering) case, which is therefore the operative regime throughout.

Definition 2 (k -sparse covering number). For $1 \leq k \leq d_i$ and $0 < \varepsilon < t$, define

$$L_i^{(k)}(\varepsilon) := \min \left\{ N : \exists \mathbf{d}_1, \dots, \mathbf{d}_N \in \mathbb{S}^{d-1} \text{ s.t. } \sup_{\mathbf{h} \in \mathcal{M}_i(t)} \min_{\substack{J \subseteq [N] \\ |J| \leq k}} \text{dist}(\mathbf{h}, \text{span}\{\mathbf{d}_j\}_{j \in J}) \leq \varepsilon \right\}.$$

We say that feature i splits at budget k whenever $L_i^{(k)}(\varepsilon) > k$.

When $L_i^{(k)}(\varepsilon) > k$, the dictionary devotes more than k columns to feature i and distinct inputs route to distinct subsets, fragmenting the feature across decoder atoms. To ensure the feature is genuinely d_i -dimensional, we assume a mild richness condition, stated using the geodesic ball $B_\gamma(\mathbf{u}_0, \rho)$ on the unit sphere centered at \mathbf{u}_0 with angular radius ρ .

Assumption 3 (Local richness). Let $t > 0$, $\dim(\mathcal{V}_i) = d_i \geq 2$. There exists $\mathbf{u}_0 \in \mathcal{V}_i \cap \mathbb{S}^{d-1}$ and $\rho \in (0, \pi)$ such that

$$t \cdot (B_\gamma(\mathbf{u}_0, \rho) \cap \mathcal{V}_i) \subseteq \mathcal{M}_i(t),$$

We next use this local cap to lower bound how many k -dimensional spans are needed to cover the feature slice.

Theorem 4 (Covering number of feature subspace). *Let $d_i \geq 2$ and Assumption 3 hold. For every $1 \leq k < d_i$ and $\varepsilon \in (0, t \sin \rho)$,*

$$L_i^{(k)}(\varepsilon) \geq C \left(\frac{t}{\varepsilon} \right)^{(d_i-k)/k}, \quad (3)$$

where $C = C(d_i, k, \rho) > 0$. When $k \geq d_i$, any orthonormal basis of \mathcal{V}_i yields $L_i^{(d_i)}(0) = d_i$ with zero error and no splitting.

The following proposition extends the same bound to the full superposition setting of Hypothesis 1.

Proposition 5 (Superposition covering number extension). *Under Hypothesis 1 with $\mu(2s-1) < 1$, $\|\boldsymbol{\xi}\|_2 \leq \eta$, and $\|\mathbf{z}_j\|_2 \leq t$, the bound (3) holds with ε replaced by $\varepsilon + \eta + \mu st$, provided the effective error remains below $t \sin \rho$.*

4.2 The SAE loss landscape rejects the basis solution

The covering bound of Section 4.1 is purely geometric. It counts *how many* atoms are needed to cover the feature slice, yet it reveals nothing about which dictionary a training run actually selects. To close that gap, we turn from counting to optimization, studying the landscape that the standard SAE objective of Equation (2) induces over the decoder alone. Recall that this objective penalizes reconstruction error together with an ℓ_1 term on the codes while constraining the decoder columns to unit norm. For a fixed decoder \mathbf{D} , the smallest loss attainable on an input \mathbf{h} over all codes is the value of the inner ℓ_1 -regularized reconstruction problem $\min_{\mathbf{a}(\mathbf{h})} \frac{1}{2} \|\mathbf{h} - \mathbf{D}\mathbf{a}(\mathbf{h})\|_2^2 + \lambda \|\mathbf{a}(\mathbf{h})\|_1$, and averaging this value over $\mathbf{h} \sim \mathcal{D}$ defines the decoder risk $R(\mathbf{D}) = \mathbb{E}_{\mathbf{h} \sim \mathcal{D}} [\min_{\mathbf{a}(\mathbf{h})} \frac{1}{2} \|\mathbf{h} - \mathbf{D}\mathbf{a}(\mathbf{h})\|_2^2 + \lambda \|\mathbf{a}(\mathbf{h})\|_1]$ over the unit-norm column manifold $\mathcal{D}_m = \{\mathbf{D} \in \mathbb{R}^{d \times m} : \|\mathbf{d}_j\|_2 = 1 \forall j\}$. This risk is the exact value of the SAE objective at its best code on each input. Any encoder, whether amortized or solved exactly, must produce codes whose loss is at least this inner minimum, and so $R(\mathbf{D})$ lower bounds the training loss of every SAE that uses the decoder \mathbf{D} . As we show, on a genuinely multi-dimensional feature, the objective does not merely tolerate splitting but *actively drives* the decoder \mathbf{D} into it, rejecting the true basis as a solution. To make this precise we specialize the decoder risk $R(\mathbf{D})$ to the single-feature slice, which yields

$$R(\mathbf{D}) := \mathbb{E}_{\mathbf{h} \sim \mathcal{D}} \left[\min_{\mathbf{a}(\mathbf{h}) \in \mathbb{R}^m} \frac{1}{2} \|\mathbf{h} - \mathbf{D}\mathbf{a}(\mathbf{h})\|_2^2 + \lambda \|\mathbf{a}(\mathbf{h})\|_1 \right], \quad \mathbf{h} = t\mathbf{u}, \quad \mathbf{u} \sim \text{Uniform}(\mathbb{S}^{d_i-1} \cap \mathcal{V}_i). \quad (4)$$

Now we analyze the risk at the true basis decoder $\mathbf{D}_{\text{basis}} = [\mathbf{v}_1, \dots, \mathbf{v}_{d_i}]$. Because its columns are orthonormal, the loss decouples into d_i independent scalar soft-thresholding problems, each solved by $a_k^* = \text{sign}(u_k)(t|u_k| - \lambda)_+$ (Lemma 17). Consider the full-activation set $\mathcal{A} = \{\mathbf{u} \in \mathbb{S}^{d_i-1} : |u_k| > \lambda/t \forall k\}$, a positive-measure region on which every coordinate clears the threshold and is therefore shrunk so that its residual is exactly $\text{sign}(u_k)\lambda$. Summing these orthogonal per-coordinate residuals across all d_i directions, the residual collapses to

$$r(\mathbf{h}) = \lambda \sum_{k=1}^{d_i} \text{sign}(u_k) \mathbf{v}_k. \quad (5)$$

On each sign orthant of \mathcal{A} the residual $r(\mathbf{h})$ is constant, with norm $\|r(\mathbf{h})\|_2 = \lambda\sqrt{d_i}$, which is above the residual λ that a single aligned atom with \mathbf{h} would leave. Because $\|r(\mathbf{h})\|_2$ is the maximal correlation of $r(\mathbf{h})$ with any unit direction, a single non-basis direction aligned with that orthant attains correlation $\lambda\sqrt{d_i} > \lambda$ at every point of it, so as we show in Theorem 6, the inactivity certificate for a non-basis atom fails on a set of positive measure.

Theorem 6 (Dual certificate violation). *Let $d_i \geq 2$ and $\lambda \in (0, t)$. For any $\tilde{\mathbf{d}} \in \text{col}(\mathbf{D}_{\text{basis}})$ with basis coordinates $\mathbf{c} = (c_1, \dots, c_{d_i})^\top$, $\|\mathbf{c}\|_2 = 1$, $\tilde{\mathbf{d}} \neq \pm \mathbf{v}_k \forall k$, for $\mathbf{h} = t\mathbf{u}$, the inactivity certificate for $\tilde{\mathbf{d}}$ is violated on the aligned orthant $\mathcal{U}_{\mathbf{c}} = \{\mathbf{u} \in \mathcal{A} : \text{sign}(u_k) = \text{sign}(c_k)\}$:*

$$\tilde{\mathbf{d}}^\top r(\mathbf{h}) = \lambda \|\mathbf{c}\|_1 > \lambda. \quad (6)$$

This certificate violation means that adding a non-basis decoder direction $\tilde{\mathbf{d}}$ can lower the risk on a positive-measure set of activations. We next turn this local violation into a strict risk decrease and then into instability of the basis dictionary.

Proposition 7 (Strict risk reduction). *Under the assumptions of Theorem 6, let $\mathbf{D} = [\mathbf{D}_{\text{basis}}, \tilde{\mathbf{d}}]$. Then*

$$R(\mathbf{D}_{\text{basis}}) - R(\mathbf{D}) \geq \frac{\lambda^2}{2} (\|\mathbf{c}\|_1 - 1)^2 > 0. \quad (7)$$

Theorem 8 (Basis instability). *Let $2 \leq d_i < m$ and λ/t sufficiently small. For any $\mathbf{D}_0 \in \mathcal{D}_m$ whose first d_i columns form an orthonormal basis of \mathcal{V}_i and an extra column inactive on the all-positive orthant U^+ , let $\mathbf{D}(\alpha)$ be the path obtained by rotating that column toward $\tilde{\mathbf{d}} = \frac{1}{\sqrt{d_i}} \sum_{k=1}^{d_i} \mathbf{v}_k$, and write $f(\alpha) = \mathbf{d}_j(\alpha)^\top r(\mathbf{h})/\lambda$ for $\mathbf{h} = t\mathbf{u}$, $\mathbf{u} \in U^+$, with f increasing from $f(0) \leq 1$ to $\sqrt{d_i} > 1$ and $\alpha_0 := \inf\{\alpha \geq 0 : f(\alpha) \geq 1\}$ the boundary-crossing angle. Then $R(\mathbf{D}(\alpha)) = R(\mathbf{D}_0)$ for $\alpha \in [0, \alpha_0]$, while for every $\alpha > \alpha_0$*

$$R(\mathbf{D}_0) - R(\mathbf{D}(\alpha)) \geq 2^{-(d_i+1)} \lambda^2 (f(\alpha) - 1)^2 > 0. \quad (8)$$

In particular, there is a continuous path from \mathbf{D}_0 to strictly lower risk, so \mathbf{D}_0 is not a minimizer of R on \mathcal{D}_m .

Iterating the dual-certificate argument, every new non-basis column captures a patch of \mathbb{S}^{d_i-1} on which the certificate was violated, and the KKT conditions stabilize only once every direction lies within angular distance $O(\lambda/t)$ of some column. Covering the sphere to this resolution forces $N = \Theta((t/\lambda)^{d_i-1})$ atoms, exactly the $k = 1, \varepsilon = \lambda$ instance of the lower bound in Theorem 4. Geometry and optimization dynamics align perfectly here. The exponential blow-up, which according to Theorem 4 is geometrically necessary, is the regime toward which the standard SAE objective converges. This means that feature splitting is not just an avoidable artifact of the training process; it is the optimum that the objective function selects. As a result, the model fragments a single d_i -dimensional feature across exponentially many near-collinear atoms.

Remark 9. *As noted earlier, Bhalla et al. [2026] formalized concept manifold capture for SAEs and proved that an idealized sparse decoder over an incoherent dictionary recovers the manifold subspace. Empirically, however, they observed that trained SAEs fall short of this ideal and settle instead into a fragmented regime they term dilution, leaving open why the objective should favor such a solution over the compact decoder their theory shows to be feasible. Theorem 8 closes this gap by showing rigorously that the coordinate-wise ℓ_1 penalty makes the true subspace basis unstable and actively prefers a fragmented cover over the compact decoder and drives trained dictionaries into this regime.*

5 Subspace-Aware Sparse Autoencoders

Section 4 established that a standard SAE cannot represent a multi-dimensional feature without splitting it, because tying each latent to a single decoder direction and penalizing the code coordinate by coordinate makes a feature of intrinsic dimension d_i cheapest when split over $\Theta((t/\lambda)^{d_i-1})$ near-collinear atoms. We now fix this problem with Subspace-Aware Sparse Autoencoders (SASA), which consider a subspace as the unit of representation through block decoders \mathbf{D}_k and move sparsity to the level of blocks, so that one block carries an entire feature at the price of a single active latent. All proofs are deferred to Appendix A.2

Model. Let $\mathbf{h} \in \mathbb{R}^d$ denote the input and let $m = Kr$ be the latent dimension. We parameterize an encoder $p(\mathbf{h}) = \mathbf{E}\mathbf{h} \in \mathbb{R}^m$ with $\mathbf{E} = [\mathbf{E}_1^\top \dots \mathbf{E}_K^\top]^\top \in \mathbb{R}^{m \times d}$ and $\mathbf{E}_k \in \mathbb{R}^{r \times d}$, so that the pre-activations partition as $p_k(\mathbf{h}) = \mathbf{E}_k \mathbf{h} \in \mathbb{R}^r$. The Top- s gate $\mathcal{T}_s(\mathbf{h}) \in \arg \max_{T \subset [K], |T|=s} \sum_{k \in T} \|p_k(\mathbf{h})\|_2$ keeps the s groups of largest norm and the block-sparse latent is

$$a_k(\mathbf{h}) = \begin{cases} p_k(\mathbf{h}), & k \in \mathcal{T}_s(\mathbf{h}), \\ \mathbf{0}, & \text{otherwise.} \end{cases}$$

The decoder is block-columned $\mathbf{D} = [\mathbf{D}_1 \dots \mathbf{D}_K] \in \mathbb{R}^{d \times m}$ with $\mathbf{D}_k \in \mathbb{R}^{d \times r}$, and the reconstruction is $\mathbf{D}a(\mathbf{h}) = \sum_{k=1}^K \mathbf{D}_k a_k(\mathbf{h})$. Because \mathcal{T}_s ranks groups solely by the scalar $\|p_k(\mathbf{h})\|_2$ and the construction charges no per-coordinate penalty inside a group, it removes the root cause of sparsity penalty that Section 4.2 identified as the source of splitting.

Objective. We train SASA on activations \mathcal{S} by minimizing the reconstruction error under the Top- s block-sparse gate together with a spectral regularizer acting on each block reconstruction map,

$$\min_{\mathbf{E}, \mathbf{D}} \sum_{i=1}^n \|\mathbf{h}_i - \mathbf{D}a(\mathbf{h}_i)\|_2^2 + \lambda_{\dim} \sum_{k=1}^K \|\mathbf{D}_k \mathbf{E}_k\|_* . \quad (9)$$

The regularizer in Equation(9) acts on the spectrum of the reconstruction map $\mathbf{W}_k = \mathbf{D}_k \mathbf{E}_k$, and this is what binds the block penalty to a benign optimization geometry. The map nuclear norm admits the variational factorization $\|\mathbf{D}_k \mathbf{E}_k\|_* = \min_{\mathbf{D}_k \mathbf{E}_k = \mathbf{W}_k} \frac{1}{2} (\|\mathbf{D}_k\|_F^2 + \|\mathbf{E}_k\|_F^2)$, which is exactly the symmetric weight decay of a regularized linear autoencoder, so each active block inherits the landscape that [Kumin et al. \[2019\]](#) characterize and in which every local minimizer is global. Penalizing the spectrum of \mathbf{W}_k in this way lets a group commit only as many effective dimensions as the feature actually occupies and drives the rest toward zero, which is precisely the behavior that recovers a coherent subspace.

The objective we optimize in practice realizes this principle through a computationally efficient evaluation of the same penalty. Rather than forming an explicit SVD for every group at every step, we evaluate the penalty in batch through the Gram trace identity $\sum_{j=1}^r \sigma_j(\mathbf{W}_k) = \text{tr}((\mathbf{W}_k^\top \mathbf{W}_k)^{1/2})$. A dead-group auxiliary loss [[Gao et al., 2024](#)] keeps under-selected groups alive, and we treat it as a stabilization heuristic and defer more details on it to [Appendix C.1](#) along with the full training and inference pseudo-code in [Appendix C.2](#).

Capacity for capturing the feature. We first show that a single block of sufficient width can contain the feature.

Proposition 10 (SASA on a single-feature slice). *Fix $i \in \mathcal{I}$ and suppose $\dim(\mathcal{V}_i) = d_i \geq 1$. If SASA uses block size $r \geq d_i$ and Top- s gating with $s = 1$, then there exist decoder blocks $\{\mathbf{D}_k\}_{k=1}^K$ and some $k^* \in [K]$ such that $\sup_{\mathbf{h} \in \mathcal{M}_i(t)} \text{dist}(\mathbf{h}, \text{col}(\mathbf{D}_{k^*})) = 0$. In particular, $L_i^{(d_i)}(0) = d_i$.*

The SASA objective selects a single block. [Proposition 10](#) shows that a block of width $r \geq d_i$ can carry the feature, yet capacity does not determine the learned representation. [Section 4.2](#) established the analogous capacity for the standard SAE while proving that its objective drives the dictionary away from it, and the SASA objective reverses this conclusion. Consider the population objective on the slice,

$$R(\mathbf{E}, \mathbf{D}) = \mathbb{E}_{\mathbf{h} \sim \mathcal{M}_i(t)} \|\mathbf{h} - \mathbf{D}a(\mathbf{h})\|_2^2 + \lambda_{\dim} \sum_k \|\mathbf{W}_k\|_* .$$

The Top-1 gate routes each activation $\mathbf{h} \in \mathcal{M}_i(t)$ to a single block, so the population objective separates into one independent term per block. The term for block k depends on the data only through the second moment $\mathbf{M}_k = \mathbb{E}[\mathbf{h} \mathbf{h}^\top \mathbb{1}\{\mathbf{h} \text{ routed to } k\}]$ of the activations it receives, and its minimized value is a strictly concave spectral function of \mathbf{M}_k . Any block that captures a positive-measure share of the slice sees activations spanning the whole of \mathcal{V}_i , so its \mathbf{M}_k has full rank d_i . If a single block carries the entire slice, its moment would be $\Sigma_i = \frac{t^2}{d_i} \mathbf{P}_{\mathcal{V}_i}$, and in the regime $0 < \lambda_{\dim} < t^2/d_i$ its reconstruction map spans \mathcal{V}_i at effective rank d_i .

These moments obey the conservation law $\sum_k \mathbf{M}_k = \Sigma_i$, which fixes the total spectral budget independently of how the slice is divided among blocks. Because the per-block cost is strictly concave and every active block spans the common subspace \mathcal{V}_i , the Rotfel'd trace inequality bounds the aggregate cost of any fragmented allocation strictly above its value at Σ_i , the cost of assigning all of $\mathcal{M}_i(t)$ to a single block. Consolidating the budget onto one block therefore attains a strictly lower value of R than any allocation that activates two or more blocks.

Theorem 11 (Block recovery on the slice). *Fix $i \in \mathcal{I}$ with $\dim(\mathcal{V}_i) = d_i \geq 2$, let SASA use block size $r \geq d_i$ and Top- s gating with $s = 1$, and fix $0 < \lambda_{\dim} < t^2/d_i$. Let R denote the population objective over $\mathcal{M}_i(t)$. Then every global minimizer of R activates a single block k^* , whose decoder recovers the feature subspace, $\text{col}(\mathbf{D}_{k^*}) = \mathcal{V}_i$, with its d_i columns spanning the top- d_i eigenspace of Σ_i , and any two global minimizers differ only by the index k^* and an orthogonal rotation within \mathcal{V}_i .*

This inverts the mechanism of [Section 4.2](#). There, the separable ℓ_1 penalty acted coordinatewise and left a residual of fixed norm $\lambda\sqrt{d_i}$ on the full-activation orthant, which no basis atom could absorb and which certified a strict descent direction away from the d_i -dimensional basis into the exponential line-covering regime. The group nuclear norm couples a block's coordinates into a single concave spectral cost, and

that concavity makes any redistribution of the fixed budget Σ_i across blocks strictly more expensive. The configuration the ℓ_1 objective rejected as unstable is exactly the unique global optimum under the spectral penalty.

From the slice to superposition. For $s > 1$ concurrently active features under Hypothesis 1, the gate must recover the correct s -block support, a projection identical to block iterative hard thresholding whose exactness Eldar and Mishali [2008], Eldar et al. [2010] certify precisely under the assumed $s < \frac{1}{2}(1 + \frac{1}{\mu})$, with sub-coherence vanishing by orthonormality of each \mathbf{V}_i .

6 Sample Complexity Efficiency

A major practical limitation of SAEs is their high training cost. This bottleneck stems from the nature of the training data, since *each* input activation \mathbf{h} is not drawn from a static dataset but produced by a forward pass through an LLM that extracts an intermediate representation at a specified layer. Generating every training example therefore incurs the cost of an LLM inference, and data acquisition itself becomes the dominant. For example, on Mistral-7B, collecting hook activations for 1M tokens takes ≈ 196.8 s, compared with only ≈ 3.3 s for SAE forward and 4.6s for SAE backward passes. We show that SASA attains the same recovery guarantee from markedly fewer activations than a splitting SAE, which directly reduces the number of forward passes and the end-to-end training time. To begin, we first derive the lower bound for a standard SAE. All proofs are provided in Appendix A.3

Proposition 12. *Consider a standard SAE with decoders $\mathbf{d}_1, \dots, \mathbf{d}_N \in \mathbb{S}^{d-1}$, co-activation budget $k = 1$, and routing rule $J(\mathbf{h}) \in \arg \min_{j \in [N]} \text{dist}(\mathbf{h}, \text{span}(\mathbf{d}_j))$. Let C_j denote the number of training samples $\mathbf{h}_1, \dots, \mathbf{h}_n$ routed to index j . Fix $\delta \in (0, 1)$. If $n < N(\log N + \log(\frac{1}{\delta}))$, then with probability at least δ there exists some $j \in [N]$ such that $C_j = 0$.*

Now, we turn to quantifying the sample complexity of SASA. As shown in Theorem 11, the SASA minimizer places the entire feature in one block whose map has column space \mathcal{V}_i , so the SASA estimator on the slice is the top- d_i eigenspace of the empirical second moment and the recovery problem is exactly principal subspace estimation, for which the sample complexity is provided in the below theorem.

Theorem 13. *Fix feature $i \in \mathcal{I}$ and its subspace $\mathcal{V}_i \subset \mathbb{R}^d$ with intrinsic dimension $d_i = \dim(\mathcal{V}_i) \geq 2$ and radius $t > 0$. Let $\mathbf{h}_1, \dots, \mathbf{h}_n$ be i.i.d. samples from $\mathcal{M}_i(t)$ with $\|\mathbf{h}_i\|_2 = t$, let $\widehat{\Sigma}_i := \frac{1}{n} \sum_{j=1}^n \mathbf{h}_j \mathbf{h}_j^\top$, and let $\widehat{\mathcal{V}}_i$ be the span of the top d_i eigenvectors of $\widehat{\Sigma}_i$. Then for any $\varepsilon \in (0, t)$ and $\delta \in (0, 1)$, if $n \geq 128 d_i^2 \log(\frac{2d}{\delta}) \frac{t^2}{\varepsilon^2}$, then with probability at least $1 - \delta$, $\sup_{\mathbf{h} \in \mathcal{M}_i(t), \|\mathbf{h}\|_2=t} \text{dist}(\mathbf{h}, \widehat{\mathcal{V}}_i) \leq \varepsilon$.*

This result highlights a sample complexity bottleneck induced by splitting. SASA learns the subspace \mathcal{V}_i holistically, requiring $n \geq 128 d_i^2 \log(\frac{2d}{\delta}) \frac{t^2}{\varepsilon^2}$ samples—a polynomial dependence on d_i (Theorem 13). In contrast, for a standard SAE to achieve error ε , the number of directions must scale as $N \geq C(\frac{t}{\varepsilon})^{d_i-1}$ —the $k = 1$ (line-covering) instance of the general $\Omega((\frac{t}{\varepsilon})^{(d_i-k)/k})$ bound (Theorem 4)—and Proposition 12 requires $n \geq N \log N$ samples to ensure every direction is trained.

Since the cost of data acquisition scales linearly with n , and each sample requires a forward pass of the LLM, reducing sample complexity directly lowers the end-to-end training cost. Under mild structural assumptions that the underlying features admit a multi-dimensional latent structure, accurate recovery needs fewer activations and thus fewer LLM forward passes.

7 Experiments

In this section, we conduct experiments on real LLMs to evaluate how SASA helps efficient training, monosemanticity, and interpretability.

7.1 Experimental setup

LLMs and training signal. We train SASA on residual-stream activations from two pretrained LLMs: GPT-2 Small ($d = 768$) and Mistral-7B-v0.1 ($d = 4096$). Following standard SAE practice, we (i) sample text from a large web corpus, (ii) run the frozen LLM and cache residual-stream activations at a fixed mid-layer SAE hook, and (iii) optimize an autoencoder on the resulting activation stream. All experiments were run on 1 A100 80GB GPU.

Table 1: Core results for SAE and SASA.

Metric	GPT-2		Mistral-7B	
	Standard	SASA	Standard	SASA
Training Token Budget	300M	150M	1B	500M
KL Score	98.0%	97.0%	93.2%	95.3%
CE Score	98.0%	97.0%	94.1%	95.1%
Frac. Explained Variance	99.1%	98.8%	96.7%	98.6%
Sparsity (ℓ_0)	60	60	285	80

Table 2: Feature absorption on the first-letter benchmark of Chanin et al. [2025]. Lower is better.

Metric	GPT-2		Mistral-7B	
	Standard	SASA	Standard	SASA
Mean frac. absorption	37.2%	6.6%	24.0%	18.3%
Full frac. absorption	49.6%	4.7%	23.3%	11.9%

Table 3: GPT-2 layer 7 comparison across SAE architectures, all trained on the same data and token budget. Best in each column is **bold**; second-best is underlined.

Model	AutoInterp \uparrow	Mean Absorption \downarrow	Frac. Var. Expl. \uparrow
ReLU SAE	0.710	0.267	1.000
JumpReLU SAE	0.698	0.553	1.000
Gated SAE	0.669	0.240	1.000
TopK SAE	0.831	<u>0.114</u>	0.993
BatchTopK SAE	0.840	0.192	0.993
TopK-SASA	<u>0.833</u>	0.046	0.989

Training protocol. We conduct two types of comparisons. First, to test sample efficiency, we train SASA with roughly half the token budget of the standard externally trained SAEs [Bloom et al., 2024, Engels et al., 2025] on both GPT-2 and Mistral (Tables 1 and 2). Second, to isolate the effect of architecture, we train SASA and all scalar baselines on GPT-2 with the same data, token budget, and optimization schedule (Table 3). Full training details are provided in Appendix B.

Baselines. We compare against ReLU [Bricken et al., 2023], Gated [Rajamanoharan et al., 2024a], JumpReLU [Rajamanoharan et al., 2024b], TopK [Gao et al., 2024], BatchTopK [Bussmann et al., 2024] and the Mistral SAE from Engels et al. [2025].

7.2 Core metrics and baseline comparisons

Section 6 predicts that SASA requires fewer activations to recover feature structure than standard SAEs. To test this, we train SASA with half the token budget of the corresponding standard SAEs (GPT-2: 150M vs 300M; Mistral: 500M vs 1B). Table 1 shows that SASA matches or exceeds standard SAE performance on KL score [Braun et al., 2024], CE score [Rajamanoharan et al., 2024a], explained variance, and sparsity across both models, providing empirical support for the sample-complexity advantage.

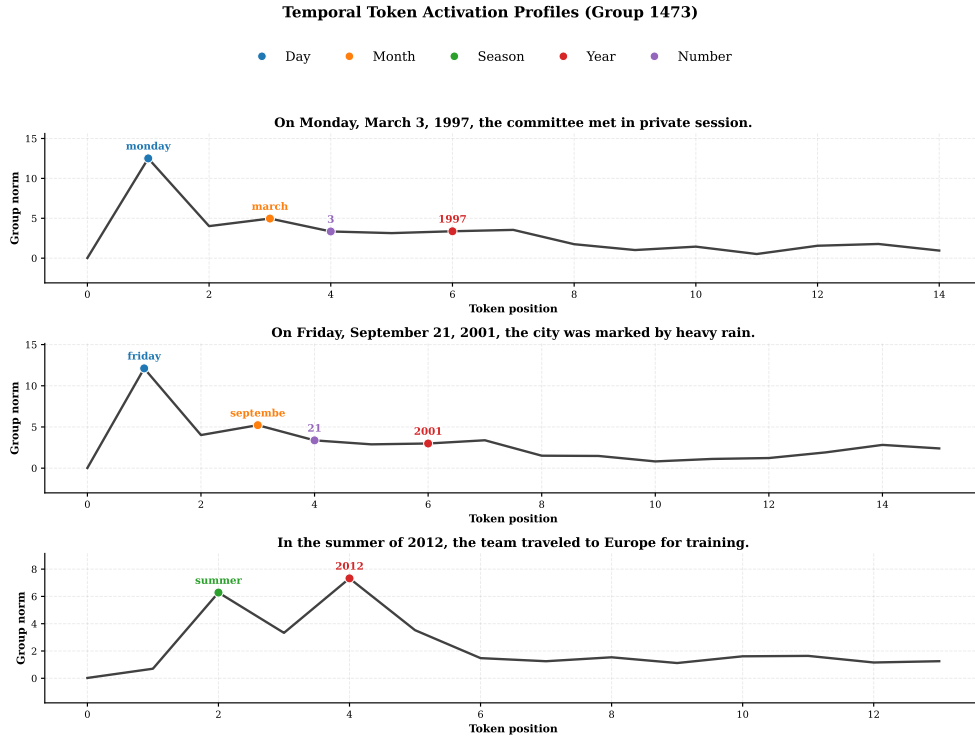
Beyond reconstruction, the key question is whether SASA improves monosemanticity. *Feature absorption*—where a child latent absorbs its parent’s direction while the parent develops a “hole”—is a failure mode closely linked to splitting, since distributing a feature across multiple latents facilitates direction migration. Table 2 evaluates absorption via the first-letter benchmark [Chanin et al., 2025] (details in Appendix F.1), showing that SASA substantially reduces absorption on both models (GPT-2: 6.6% vs 37.2%; Mistral: 18.3% vs 24.0%).

TopK-SASA achieves the best overall balance with 0.833 AutoInterp and only 0.046 mean absorption. BatchTopK is the only baseline with marginally higher AutoInterp (0.840), but at $4\times$ higher absorption (0.192).

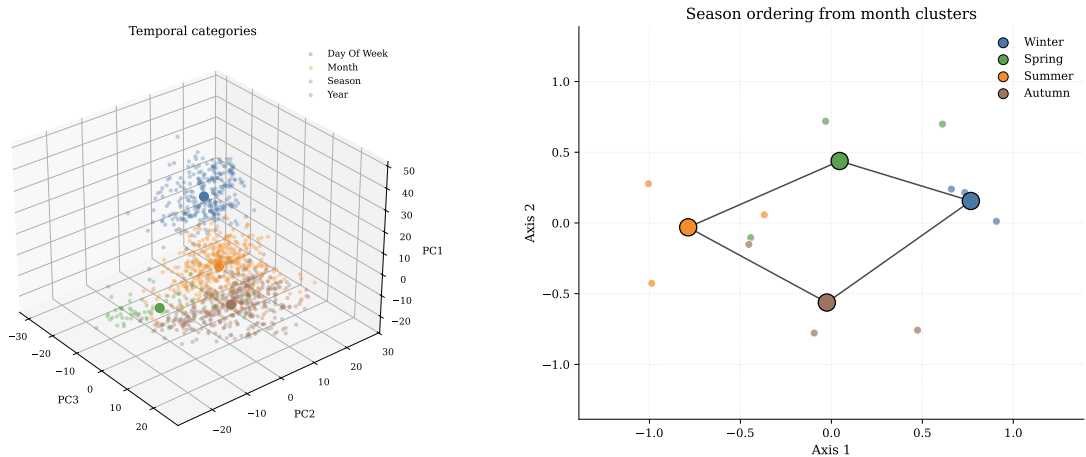
7.3 Interpretability

The temporal concepts examined below occupy a genuinely low-dimensional subspace in raw GPT-2 activations ($\text{dim}_{90} = 14$ out of 768 dimensions, without any SAE; see Appendix D), confirming the structural assumption underlying our theoretical analysis. Engels et al. [2025] found that standard SAEs learn fragmented clusters of decoder atoms for these concepts: 9 atoms for days, 16 for months, and 10 for years, totaling 35 atoms. We find that GPT-2 SASA *Group 1473* captures a *universal* set of temporal relations within a single decoder group of 6 vectors, consolidating what standard SAEs fragment across 35 directions.

We illustrate this in Figures 3a–3c. The group acts as a general temporal detector (Figure 3a), firing consistently on days, months, years, and seasons within a natural context. Crucially, the subspace



(a) **Group 1473 activations.** Consistent responses to temporal concepts.



(b) **Temporal subspace.** PCA separates days, months, seasons, and years.

(c) **Cyclic topology.** The learned subspace recovers seasonal order.

preserves the geometry of these features. PCA visualization (Figure 3b) separates temporal categories into distinct regions, and the subspace recovers the inherent cyclic topology of time (Figure 3c). These subspaces extend beyond temporal and geographical concepts, with Appendix H presenting a sports subspace (Group 1056). Geographical analysis appears in Appendix G; for the complete methodology, see Appendix F.2.

8 Conclusion

We introduced Subspace-Aware Sparse Autoencoders (SASA), which replace single-decoder directions with learned decoder subspaces and enforce structured sparsity at the group level for mechanistic interpretability of LLMs. We provided theoretical motivation for why vector dictionaries can split multi-dimensional concepts (leading to feature splitting), how this is not only a necessity geometrically, but a preference in the optimization dynamics of SAEs, and why subspace groups can represent them more faithfully. We also rigorously show the gain in sample efficiency needed for training SASA compared

to standard SAE.

Future work. We plan to study whether SASA generalizes across model families, guided by ideas such as the Platonic Representation Hypothesis [Huh et al., 2024] and the Universal Weight Subspace Hypothesis [Kaushik et al., 2025]. If subspaces align across models, they could enable the transfer of interpretability structure and reduce repeated effort. We also aim to recover meaningful internal coordinates within each learned subspace and use them for inference-time steering and intervention. This direction explicitly leverages the richer geometry of LLM representations and may help address known robustness and generalization issues in steering, as discussed in Tan et al. [2025].

Limitations. Despite the strengths of our approach, this work has several limitations that merit discussion. First, although SASA cuts training cost substantially, the remaining compute is still too high for very large LLMs. Collecting enough activations and training at scale would still take considerable time and resources. Second, learning a feature *subspace* does not automatically yield an interpretable coordinate system inside that subspace. We can identify the span, but we do not yet know how different feature values are organized within it, and our current analysis often relies on manual inspection.

References

- Guillaume Alain and Yoshua Bengio. Understanding intermediate layers using linear classifier probes. (arXiv:1610.01644), November 2018. doi:10.48550/arXiv.1610.01644. URL <http://arxiv.org/abs/1610.01644>. arXiv:1610.01644.
- Andy Ardit, Oscar Obeso, Aaquib Syed, Daniel Paleka, Nina Panickssery, Wes Gurnee, and Neel Nanda. Refusal in language models is mediated by a single direction. (arXiv:2406.11717), October 2024. doi:10.48550/arXiv.2406.11717. URL <http://arxiv.org/abs/2406.11717>. arXiv:2406.11717.
- Usha Bhalla, Thomas Fel, Can Rager, Sheridan Feucht, Tal Haklay, Daniel Wurgaft, Siddharth Boppana, Matthew Kowal, Vasudev Shyam, Jack Merullo, et al. Do sparse autoencoders capture concept manifolds? *arXiv preprint arXiv:2604.28119*, 2026.
- Joseph Bloom, Curt Tigges, Anthony Duong, and David Chanin. Saelens. <https://github.com/decoderresearch/SAELens>, 2024.
- Jean-Christophe Bourin. A matrix subadditivity inequality for symmetric norms. *Proceedings of the American Mathematical Society*, 138(2):495–504, 2010.
- Dan Braun, Jordan Taylor, Nicholas Goldowsky-Dill, and Lee Sharkey. Identifying functionally important features with end-to-end sparse dictionary learning. (arXiv:2405.12241), May 2024. doi:10.48550/arXiv.2405.12241. URL <http://arxiv.org/abs/2405.12241>. arXiv:2405.12241.
- Trenton Bricken, Adly Templeton, Joshua Batson, Brian Chen, Adam Jermyn, Tom Conerly, Nick Turner, Cem Anil, Carson Denison, Amanda Askeel, Robert Lasenby, Yifan Wu, Shauna Kravec, Nicholas Schiefer, Tim Maxwell, Nicholas Joseph, Zac Hatfield-Dodds, Alex Tamkin, Karina Nguyen, Brayden McLean, Josiah E Burke, Tristan Hume, Shan Carter, Tom Henighan, and Christopher Olah. Towards monosemanticity: Decomposing language models with dictionary learning. *Transformer Circuits Thread*, 2023.
- Bart Bussmann, Patrick Leask, and Neel Nanda. Batchtopk sparse autoencoders. (arXiv:2412.06410), December 2024. doi:10.48550/arXiv.2412.06410. URL <http://arxiv.org/abs/2412.06410>. arXiv:2412.06410.
- Bart Bussmann, Noa Nabeshima, Adam Karvonen, and Neel Nanda. Learning multi-level features with matryoshka sparse autoencoders. (arXiv:2503.17547), March 2025. doi:10.48550/arXiv.2503.17547. URL <http://arxiv.org/abs/2503.17547>. arXiv:2503.17547.
- Emmanuel J. Candès and Benjamin Recht. Exact matrix completion via convex optimization. *Foundations of Computational Mathematics*, 9(6):717–772, December 2009. ISSN 1615-3383. doi:10.1007/s10208-009-9045-5. URL <https://doi.org/10.1007/s10208-009-9045-5>.

- David Chazin, James Wilken-Smith, Tomáš Dulka, Hardik Bhatnagar, Satvik Golechha, and Joseph Bloom. A is for absorption: Studying feature splitting and absorption in sparse autoencoders, 2025. URL <https://arxiv.org/abs/2409.14507>.
- Arthur Conmy, Augustine N. Mavor-Parker, Aengus Lynch, Stefan Heimersheim, and Adrià Garriga-Alonso. Towards automated circuit discovery for mechanistic interpretability. In *Proceedings of the 37th International Conference on Neural Information Processing Systems*, NIPS '23, Red Hook, NY, USA, 2023. Curran Associates Inc.
- Feng Dai. *Approximation theory and harmonic analysis on spheres and balls*. Springer, 2013.
- Aristides V. Doumas and Vassilis G. Papanicolaou. The coupon collector’s problem revisited: Generalizing the double dixie cup problem of newman and shepp. (arXiv:1412.3626), November 2015. doi:10.48550/arXiv.1412.3626. URL <http://arxiv.org/abs/1412.3626>. arXiv:1412.3626.
- Yonina C Eldar and Moshe Mishali. Robust recovery of signals from a structured union of subspaces. *arXiv preprint arXiv:0807.4581*, 2008.
- Yonina C Eldar, Patrick Kuppinger, and Helmut Bolcskei. Block-sparse signals: Uncertainty relations and efficient recovery. *IEEE Transactions on Signal Processing*, 58(6):3042–3054, 2010.
- Nelson Elhage, Tristan Hume, Catherine Olsson, Nicholas Schiefer, Tom Henighan, Shauna Kravec, Zac Hatfield-Dodds, Robert Lasenby, Dawn Drain, Carol Chen, Roger Grosse, Sam McCandlish, Jared Kaplan, Dario Amodei, Martin Wattenberg, and Christopher Olah. Toy models of superposition. *Transformer Circuits Thread*, 2022.
- Joshua Engels, Eric J. Michaud, Isaac Liao, Wes Gurnee, and Max Tegmark. Not all language model features are one-dimensionally linear. (arXiv:2405.14860), February 2025. doi:10.48550/arXiv.2405.14860. URL <http://arxiv.org/abs/2405.14860>. arXiv:2405.14860.
- Leo Gao, Stella Biderman, Sid Black, Laurence Golding, Travis Hoppe, Charles Foster, Jason Phang, Horace He, Anish Thite, Noa Nabeshima, Shawn Presser, and Connor Leahy. The pile: An 800gb dataset of diverse text for language modeling. (arXiv:2101.00027), December 2020. doi:10.48550/arXiv.2101.00027. URL <http://arxiv.org/abs/2101.00027>. arXiv:2101.00027.
- Leo Gao, Tom Dupré la Tour, Henk Tillman, Gabriel Goh, Rajan Troll, Alec Radford, Ilya Sutskever, Jan Leike, and Jeffrey Wu. Scaling and evaluating sparse autoencoders. (arXiv:2406.04093), 2024. doi:10.48550/arXiv.2406.04093. URL <http://arxiv.org/abs/2406.04093>. arXiv:2406.04093.
- Jorge García-Carrasco, Alejandro Maté, and Juan Trujillo. Detecting and understanding vulnerabilities in language models via mechanistic interpretability. In *Proceedings of the Thirty-Third International Joint Conference on Artificial Intelligence*, IJCAI '24, 2024. ISBN 978-1-956792-04-1. doi:10.24963/ijcai.2024/43. URL <https://doi.org/10.24963/ijcai.2024/43>.
- Aaron Gokaslan, Vanya Cohen, Ellie Pavlick, and Stefanie Tellex. Openwebtext corpus, 2019. URL <http://Skylion007.github.io/OpenWebTextCorpus>.
- Zellig S. Harris. Distributional structure. *WORD*, 10(2–3):146–162, August 1954. ISSN 0043-7956, 2373-5112. doi:10.1080/00437956.1954.11659520. URL <http://www.tandfonline.com/doi/full/10.1080/00437956.1954.11659520>.
- Roger A. Horn and Charles R. Johnson. *Matrix Analysis*. Cambridge University Press, Cambridge, 1985. doi:10.1017/CBO9780511810817. URL <https://www.cambridge.org/core/books/matrix-analysis/9CF2CB491C9E97948B15FAD835EF9A8B>.
- Minyoung Huh, Brian Cheung, Tongzhou Wang, and Phillip Isola. The platonic representation hypothesis. (arXiv:2405.07987), 2024. doi:10.48550/arXiv.2405.07987. URL <http://arxiv.org/abs/2405.07987>. arXiv:2405.07987.
- Prakhar Kaushik, Shravan Chaudhari, Ankit Vaidya, Rama Chellappa, and Alan Yuille. The universal weight subspace hypothesis. (arXiv:2512.05117), December 2025. doi:10.48550/arXiv.2512.05117. URL <http://arxiv.org/abs/2512.05117>. arXiv:2512.05117.

- Andrew Knyazev, Abram Jujunashvili, and Merico Argentati. Angles between infinite dimensional subspaces with applications to the rayleigh–ritz and alternating projectors methods. *Journal of Functional Analysis*, 259(6):1323–1345, September 2010. ISSN 0022-1236. doi:[10.1016/j.jfa.2010.05.018](https://doi.org/10.1016/j.jfa.2010.05.018). URL <http://dx.doi.org/10.1016/j.jfa.2010.05.018>.
- Daniel Kunin, Jonathan Bloom, Aleksandrina Goeva, and Cotton Seed. Loss landscapes of regularized linear autoencoders. In *International conference on machine learning*, pages 3560–3569. PMLR, 2019.
- Patrick Leask, Neel Nanda, and Noura Al Moubayed. Inference-time decomposition of activations (itda): A scalable approach to interpreting large language models. (arXiv:2505.17769), 2025. doi:[10.48550/arXiv.2505.17769](https://doi.org/10.48550/arXiv.2505.17769). URL <http://arxiv.org/abs/2505.17769>. arXiv:2505.17769.
- Andrew Lee, Xiaoyan Bai, Itamar Pres, Martin Wattenberg, Jonathan K. Kummerfeld, and Rada Mihalcea. A mechanistic understanding of alignment algorithms: A case study on dpo and toxicity. (arXiv:2401.01967), January 2024. doi:[10.48550/arXiv.2401.01967](https://doi.org/10.48550/arXiv.2401.01967). URL <http://arxiv.org/abs/2401.01967>. arXiv:2401.01967.
- Eric J. Michaud, Liv Gorton, and Tom McGrath. Understanding sparse autoencoder scaling in the presence of feature manifolds. (arXiv:2509.02565), 2025. doi:[10.48550/arXiv.2509.02565](https://doi.org/10.48550/arXiv.2509.02565). URL <http://arxiv.org/abs/2509.02565>. arXiv:2509.02565.
- Alexander Modell, Patrick Rubin-Delanchy, and Nick Whiteley. The origins of representation manifolds in large language models. (arXiv:2505.18235), May 2025. doi:[10.48550/arXiv.2505.18235](https://doi.org/10.48550/arXiv.2505.18235). URL <http://arxiv.org/abs/2505.18235>. arXiv:2505.18235.
- Kiho Park, Yo Joong Choe, and Victor Veitch. The linear representation hypothesis and the geometry of large language models. In *Proceedings of the 41st International Conference on Machine Learning, ICML’24*. JMLR.org, 2024.
- Kiho Park, Yo Joong Choe, Yibo Jiang, and Victor Veitch. The geometry of categorical and hierarchical concepts in large language models. (arXiv:2406.01506), February 2025. doi:[10.48550/arXiv.2406.01506](https://doi.org/10.48550/arXiv.2406.01506). URL <http://arxiv.org/abs/2406.01506>. arXiv:2406.01506.
- Senthooran Rajamanoharan, Arthur Conmy, Lewis Smith, Tom Lieberum, Vikrant Varma, János Kramár, Rohin Shah, and Neel Nanda. Improving dictionary learning with gated sparse autoencoders. (arXiv:2404.16014), April 2024a. doi:[10.48550/arXiv.2404.16014](https://doi.org/10.48550/arXiv.2404.16014). URL <http://arxiv.org/abs/2404.16014>. arXiv:2404.16014.
- Senthooran Rajamanoharan, Tom Lieberum, Nicolas Sonnerat, Arthur Conmy, Vikrant Varma, János Kramár, and Neel Nanda. Jumping ahead: Improving reconstruction fidelity with jumprelu sparse autoencoders. (arXiv:2407.14435), August 2024b. doi:[10.48550/arXiv.2407.14435](https://doi.org/10.48550/arXiv.2407.14435). URL <http://arxiv.org/abs/2407.14435>. arXiv:2407.14435.
- Lee Sharkey, Bilal Chughtai, Joshua Batson, Jack Lindsey, Jeff Wu, Lucius Bushnaq, Nicholas Goldowsky-Dill, Stefan Heimersheim, Alejandro Ortega, Joseph Bloom, Stella Biderman, Adria Garriga-Alonso, Arthur Conmy, Neel Nanda, Jessica Rumbelow, Martin Wattenberg, Nandi Schoots, Joseph Miller, Eric J. Michaud, Stephen Casper, Max Tegmark, William Saunders, David Bau, Eric Todd, Atticus Geiger, Mor Geva, Jesse Hoogland, Daniel Murfet, and Tom McGrath. Open problems in mechanistic interpretability. (arXiv:2501.16496), January 2025. doi:[10.48550/arXiv.2501.16496](https://doi.org/10.48550/arXiv.2501.16496). URL <http://arxiv.org/abs/2501.16496>. arXiv:2501.16496.
- Daniel Tan, David Chanin, Aengus Lynch, Dimitrios Kanoulas, Brooks Paige, Adria Garriga-Alonso, and Robert Kirk. Analyzing the generalization and reliability of steering vectors. (arXiv:2407.12404), May 2025. doi:[10.48550/arXiv.2407.12404](https://doi.org/10.48550/arXiv.2407.12404). URL <http://arxiv.org/abs/2407.12404>. arXiv:2407.12404.
- Emmanouil Theodosis, Bahareh Tolooshams, Pranay Tankala, Abiy Tasissa, and Demba Ba. On the convergence of group-sparse autoencoders. (arXiv:2102.07003), January 2022. doi:[10.48550/arXiv.2102.07003](https://doi.org/10.48550/arXiv.2102.07003). URL <http://arxiv.org/abs/2102.07003>. arXiv:2102.07003.
- Robert Tibshirani. Regression shrinkage and selection via the lasso. *Journal of the Royal Statistical Society Series B: Statistical Methodology*, 58(1):267–288, 1996.

- Joel A. Tropp. User-friendly tail bounds for sums of random matrices. *Foundations of Computational Mathematics*, 12(4):389–434, August 2012. ISSN 1615-3383. doi:[10.1007/s10208-011-9099-z](https://doi.org/10.1007/s10208-011-9099-z). URL <https://doi.org/10.1007/s10208-011-9099-z>.
- Kevin Wang, Alexandre Variengien, Arthur Conmy, Buck Shlegeris, and Jacob Steinhardt. Interpretability in the wild: a circuit for indirect object identification in gpt-2 small. (arXiv:2211.00593), November 2022. doi:[10.48550/arXiv.2211.00593](https://doi.org/10.48550/arXiv.2211.00593). URL <http://arxiv.org/abs/2211.00593>. arXiv:2211.00593.
- Thomas Winninger, Boussad Addad, and Katarzyna Kapusta. Using mechanistic interpretability to craft adversarial attacks against large language models. (arXiv:2503.06269), May 2025. doi:[10.48550/arXiv.2503.06269](https://doi.org/10.48550/arXiv.2503.06269). URL <http://arxiv.org/abs/2503.06269>. arXiv:2503.06269.
- Y. Yu, T. Wang, and R. J. Samworth. A useful variant of the davis–kahan theorem for statisticians. *Biometrika*, 102(2):315–323, 04 2014. ISSN 0006-3444. doi:[10.1093/biomet/asv008](https://doi.org/10.1093/biomet/asv008). URL <https://doi.org/10.1093/biomet/asv008>.
- Ming Yuan and Yi Lin. Model selection and estimation in regression with grouped variables. *Journal of the Royal Statistical Society Series B: Statistical Methodology*, 68(1):49–67, February 2006. ISSN 1369-7412, 1467-9868. doi:[10.1111/j.1467-9868.2005.00532.x](https://doi.org/10.1111/j.1467-9868.2005.00532.x). URL <https://academic.oup.com/jrsssb/article/68/1/49/7110631>.

Appendix

A Proofs of Theoretical Results

This appendix collects the detailed proofs of all theorems, propositions, and lemmas stated or used in the main body.

A.1 Necessity of Subspace Learning

We introduce a few useful facts, which are key in the proof of Theorem 4 and Theorem 8. To start with, we first state some geometric preliminaries. Throughout this section, σ_n denotes the surface measure on \mathbb{S}^n and $\gamma(\mathbf{u}, \mathbf{v}) = \arccos(|\langle \mathbf{u}, \mathbf{v} \rangle|)$ denotes the projective angular distance on \mathbb{S}^{d-1} .

A.1.1 Geometric preliminaries

Lemma 14 (Subspace projection reduces distance). *For any $\mathbf{h} \in \mathcal{V}_i$ and any linear subspace $\mathbf{W} \subset \mathbb{R}^d$,*

$$\text{dist}(\mathbf{h}, \mathbf{P}_{\mathcal{V}_i} \mathbf{W}) \leq \text{dist}(\mathbf{h}, \mathbf{W}).$$

Proof. Recall that \mathcal{V}_i is the feature subspace and $\mathbf{P}_{\mathcal{V}_i}$ the orthogonal projector onto it. The claim is that projecting a competing subspace \mathbf{W} onto \mathcal{V}_i can only bring it closer to a point that already lies in \mathcal{V}_i . To see this, let \mathbf{w}^* attain the distance from \mathbf{h} to \mathbf{W} . Since $\mathbf{h} \in \mathcal{V}_i$, the decomposition $\mathbf{h} - \mathbf{w}^* = (\mathbf{h} - \mathbf{P}_{\mathcal{V}_i} \mathbf{w}^*) - \mathbf{P}_{\mathcal{V}_i^\perp} \mathbf{w}^*$ splits into orthogonal components lying in \mathcal{V}_i and \mathcal{V}_i^\perp respectively, so the Pythagorean theorem gives

$$\|\mathbf{h} - \mathbf{w}^*\|_2^2 = \|\mathbf{h} - \mathbf{P}_{\mathcal{V}_i} \mathbf{w}^*\|_2^2 + \|\mathbf{P}_{\mathcal{V}_i^\perp} \mathbf{w}^*\|_2^2 \geq \text{dist}(\mathbf{h}, \mathbf{P}_{\mathcal{V}_i} \mathbf{W})^2. \quad \square$$

Lemma 15 (Tube volume on the sphere). *Let $\mathbf{W} \subset \mathbb{R}^{d_i}$ be a k -dimensional linear subspace with $1 \leq k < d_i$, and let $\beta \in (0, \pi/2)$. Define the angular tube*

$$\text{Tube}_\beta(\mathbf{W}) = \{\mathbf{u} \in \mathbb{S}^{d_i-1} : \text{dist}(\mathbf{u}, \mathbf{W}) \leq \sin \beta\}.$$

Then

$$\sigma_{d_i-1}(\text{Tube}_\beta(\mathbf{W})) \leq C_T(d_i, k) \beta^{d_i-k}, \quad C_T(d_i, k) = \frac{\sigma_{k-1}(\mathbb{S}^{k-1}) \sigma_{d_i-k-1}(\mathbb{S}^{d_i-k-1})}{d_i - k}.$$

Proof. The bound estimates the surface area of a thin angular neighborhood of a k -dimensional subspace inside the sphere, which is the geometric quantity that limits how much of the feature slice a single k -dimensional span can cover. Without loss of generality, let $\mathbf{W} = \text{span}\{\mathbf{e}_1, \dots, \mathbf{e}_k\}$. Parameterize $\mathbf{u} \in \mathbb{S}^{d_i-1}$ as $\mathbf{u} = \cos \theta \mathbf{w} + \sin \theta \mathbf{n}$ with $\mathbf{w} \in \mathbb{S}^{k-1} \subset \mathbf{W}$, $\mathbf{n} \in \mathbb{S}^{d_i-k-1} \subset \mathbf{W}^\perp$, and $\theta \in [0, \pi/2]$. The decomposition of the surface measure adapted to the splitting $\mathbb{R}^{d_i} = \mathbf{W} \oplus \mathbf{W}^\perp$ [Dai, 2013, Lemma A.5.4], after writing the \mathbf{W}^\perp component in polar coordinates (with $m = k$, $d = d_i - k$), gives

$$d\sigma_{d_i-1}(\mathbf{u}) = \cos^{k-1} \theta \sin^{d_i-k-1} \theta d\theta d\sigma_{k-1}(\mathbf{w}) d\sigma_{d_i-k-1}(\mathbf{n}).$$

The tube condition $\text{dist}(\mathbf{u}, \mathbf{W}) = \sin \theta \leq \sin \beta$ is equivalent to $\theta \leq \beta$, the restriction $\beta \in (0, \pi/2)$ keeping \sin monotone so the two are interchangeable. Integrating and using $\cos \theta \leq 1$, $\sin \theta \leq \theta$ on $[0, \pi/2]$,

$$\sigma_{d_i-1}(\text{Tube}_\beta(\mathbf{W})) \leq \sigma_{k-1}(\mathbb{S}^{k-1}) \sigma_{d_i-k-1}(\mathbb{S}^{d_i-k-1}) \int_0^\beta \theta^{d_i-k-1} d\theta = C_T(d_i, k) \beta^{d_i-k}. \quad \square$$

Lemma 16 (Cap volume positivity). *For $d_i \geq 2$, $\mathbf{u}_0 \in \mathbb{S}^{d_i-1}$, and $\rho \in (0, \pi/2)$, there exists a constant $c_\rho = c_\rho(d_i) > 0$ such that*

$$\sigma_{d_i-1}(B_\gamma(\mathbf{u}_0, \rho)) \geq c_\rho.$$

Proof. The statement states that a geodesic cap of fixed angular radius ρ on the unit sphere carries a strictly positive amount of surface measure, a fact we use later as the area that the covering tubes must collectively account for. By rotational invariance, $\sigma_{d_i-1}(B_\gamma(\mathbf{u}_0, \rho)) = \sigma_{d_i-1}(\mathbb{S}^{d_i-2}) \int_0^\rho \sin^{d_i-2} \theta d\theta$, which is positive since the integrand is continuous and strictly positive on $(0, \rho)$. \square

A.1.2 Proof of Theorem 4

Proof. Recall that $\mathcal{M}_i(t)$ is the noiseless single-feature slice, i.e. the radius- t sphere $\{t\mathbf{u} : \mathbf{u} \in \mathbb{S}^{d-1} \cap \mathcal{V}_i\}$ inside the feature subspace \mathcal{V}_i , and that the goal is to lower bound the number N of unit decoder directions needed to ε -cover it with k -dimensional spans. Fix $1 \leq k < d_i$, set $\beta = \arcsin(\varepsilon/t) \in (0, \rho)$, where the hypothesis $\varepsilon \in (0, t \sin \rho)$ keeps the argument in range so that $\beta < \rho < \pi/2$, and let $\mathbf{d}_1, \dots, \mathbf{d}_N \in \mathbb{S}^{d-1}$ account for $L_i^{(k)}(\varepsilon) = N$. By Definition 2, every $\mathbf{h} = t\mathbf{u} \in \mathcal{M}_i(t)$ admits a subset $J \subseteq [N]$ with $|J| \leq k$ satisfying

$$\text{dist}(\mathbf{h}, \text{span}\{\mathbf{d}_j\}_{j \in J}) \leq \varepsilon.$$

Lemma 14 projects this guarantee into \mathcal{V}_i , so that with $\widetilde{\mathbf{W}}_J = \mathbf{P}_{\mathcal{V}_i} \text{span}\{\mathbf{d}_j\}_{j \in J}$ and $\dim(\widetilde{\mathbf{W}}_J) \leq k$, every $\mathbf{u} \in B_\gamma(\mathbf{u}_0, \rho) \cap \mathcal{V}_i$ lies in $\text{Tube}_\beta(\widetilde{\mathbf{W}}_J)$. The number of k -element subsets of $[N]$ is at most

$$\sum_{j=1}^k \binom{N}{j} \leq kN^k.$$

Each tube has surface measure at most $C_T(d_i, k)\beta^{d_i-k}$ by Lemma 15. The union of all tubes must cover $B_\gamma(\mathbf{u}_0, \rho) \cap \mathcal{V}_i$, so Lemma 16 gives

$$0 < c_\rho \leq kN^k \cdot C_T(d_i, k) \cdot \beta^{d_i-k}.$$

Now, rearranging and using $\sin \beta \geq \frac{2}{\pi}\beta$ on $(0, \frac{\pi}{2})$, which gives $\beta \leq \frac{\pi\varepsilon}{2t}$,

$$N^k \geq \frac{c_\rho}{kC_T} \cdot \beta^{-(d_i-k)} \geq \frac{c_\rho}{kC_T} \left(\frac{2}{\pi}\right)^{d_i-k} \left(\frac{t}{\varepsilon}\right)^{d_i-k}.$$

Taking k -th roots yields $N \geq C(d_i, k, \rho)(t/\varepsilon)^{(d_i-k)/k}$ with $C(d_i, k, \rho) = (c_\rho/kC_T)^{1/k}(2/\pi)^{(d_i-k)/k}$.

When $k = d_i$, any orthonormal basis of \mathcal{V}_i spans the full subspace, achieving $\text{dist}(\mathbf{h}, \mathcal{V}_i) = 0$ for all $\mathbf{h} \in \mathcal{M}_i(t)$ with $N = d_i$. \square

A.1.3 Proof of Proposition 5

Proof. Under Hypothesis 1, conditioning on feature i with at most s active features gives $\mathbf{h} = \mathbf{V}_i \mathbf{z}_i + \boldsymbol{\delta}$ with $\boldsymbol{\delta} = \sum_{j \neq i} \mathbf{V}_j \mathbf{z}_j + \boldsymbol{\xi}$. By Lemma 14, the count in Theorem 4 depends only on the projected spans $\widetilde{\mathbf{W}}_J = \mathbf{P}_{\mathcal{V}_i} \text{span}\{\mathbf{d}_j\}_{j \in J}$, so the slice point $\mathbf{V}_i \mathbf{z}_i$ is perturbed only by the in-subspace component $\mathbf{P}_{\mathcal{V}_i} \boldsymbol{\delta}$, which we bound first.

The μ -coherence of Hypothesis 1 is the operator-norm bound $\|\mathbf{V}_i^\top \mathbf{V}_j\|_2 \leq \mu$ for $j \neq i$. Because \mathbf{V}_i has orthonormal columns, each off-feature satisfies

$$\|\mathbf{P}_{\mathcal{V}_i} \mathbf{V}_j \mathbf{z}_j\|_2 = \|\mathbf{V}_i \mathbf{V}_i^\top \mathbf{V}_j \mathbf{z}_j\|_2 = \|\mathbf{V}_i^\top \mathbf{V}_j \mathbf{z}_j\|_2 \leq \|\mathbf{V}_i^\top \mathbf{V}_j\|_2 \|\mathbf{z}_j\|_2 \leq \mu t,$$

where the last step uses $\|\mathbf{z}_j\|_2 \leq t$. Summing over the at most $s-1$ active off-features and using $\|\mathbf{P}_{\mathcal{V}_i} \boldsymbol{\xi}\|_2 \leq \|\boldsymbol{\xi}\|_2 \leq \eta$ gives

$$\|\mathbf{P}_{\mathcal{V}_i} \boldsymbol{\delta}\|_2 \leq (s-1)\mu t + \eta \leq \mu s t + \eta.$$

Now fix a subset $J \subseteq [N]$ with $|J| \leq k$ and a point $\mathbf{p} \in \text{span}\{\mathbf{d}_j\}_{j \in J}$ with $\|\mathbf{h} - \mathbf{p}\|_2 \leq \varepsilon$. Then $\mathbf{P}_{\mathcal{V}_i} \mathbf{p} \in \widetilde{\mathbf{W}}_J$ and $\dim \widetilde{\mathbf{W}}_J \leq k$. Since $\mathbf{V}_i \mathbf{z}_i = \mathbf{P}_{\mathcal{V}_i} \mathbf{h} - \mathbf{P}_{\mathcal{V}_i} \boldsymbol{\delta}$,

$$\text{dist}(\mathbf{V}_i \mathbf{z}_i, \widetilde{\mathbf{W}}_J) \leq \|\mathbf{P}_{\mathcal{V}_i}(\mathbf{h} - \mathbf{p}) - \mathbf{P}_{\mathcal{V}_i} \boldsymbol{\delta}\|_2 \leq \|\mathbf{h} - \mathbf{p}\|_2 + \|\mathbf{P}_{\mathcal{V}_i} \boldsymbol{\delta}\|_2 \leq \varepsilon + \mu s t + \eta.$$

The projected spans thus k -cover every slice point $\mathbf{V}_i \mathbf{z}_i \in \mathcal{M}_i(t)$ to error $\varepsilon' = \varepsilon + \mu s t + \eta$. This is the in- \mathcal{V}_i covering counted in the proof of Theorem 4, so that argument applies with effective error $\varepsilon' = \varepsilon + \mu s t + \eta$ whenever $\varepsilon' < t \sin \rho$. \square

A.1.4 Basis instability

Throughout this part we work with the decoder risk $R(\mathbf{D})$ induced by the standard SAE objective. For a fixed decoder \mathbf{D} the code is chosen to minimize the inner ℓ_1 -regularized reconstruction objective $\frac{1}{2}\|\mathbf{h} - \mathbf{D}\mathbf{a}(\mathbf{h})\|_2^2 + \lambda\|\mathbf{a}(\mathbf{h})\|_1$, and $R(\mathbf{D})$ averages this best-code value over \mathbf{h} . The goal is to show that the true basis decoder is not a minimizer of this risk. We begin by computing the optimal code, and the residual it leaves, when the decoder is exactly the feature basis.

Lemma 17 (Basis residual under full activation). At $\mathbf{D}_{\text{basis}} = [\mathbf{v}_1, \dots, \mathbf{v}_{d_i}]$, the ℓ_1 -regularized reconstruction objective

$$\min_{\mathbf{a}(\mathbf{h}) \in \mathbb{R}^{d_i}} \frac{1}{2} \|\mathbf{h} - \mathbf{D}_{\text{basis}} \mathbf{a}(\mathbf{h})\|_2^2 + \lambda \|\mathbf{a}(\mathbf{h})\|_1$$

for $\mathbf{h} = t\mathbf{u}$ with $\mathbf{u} = \sum_{k=1}^{d_i} u_k \mathbf{v}_k \in \mathbb{S}^{d_i-1} \cap \mathcal{V}_i$ has the unique solution

$$a_k^* = \text{sign}(u_k)(t|u_k| - \lambda)_+, \quad k \in [d_i].$$

On the full-activation set $\mathcal{A} = \{\mathbf{u} \in \mathbb{S}^{d_i-1} : |u_k| > \lambda/t \forall k\}$, the residual is

$$r(\mathbf{h}) = \lambda \sum_{k=1}^{d_i} \text{sign}(u_k) \mathbf{v}_k, \quad \|r(\mathbf{h})\|_2 = \lambda \sqrt{d_i}.$$

Proof. Here λ/t plays the role of a normalized activation threshold, and the full-activation set \mathcal{A} is exactly the region of the slice on which every coordinate of \mathbf{u} exceeds it and is therefore left active by soft-thresholding. Orthonormality of $\{\mathbf{v}_k\}$ and $\mathbf{h} \in \mathcal{V}_i$ decouple the objective into d_i independent scalar subproblems,

$$\frac{1}{2} \|\mathbf{h} - \mathbf{D}_{\text{basis}} \mathbf{a}(\mathbf{h})\|_2^2 + \lambda \|\mathbf{a}(\mathbf{h})\|_1 = \sum_{k=1}^{d_i} \left[\frac{1}{2} (tu_k - a_k)^2 + \lambda |a_k| \right],$$

each solved by the proximal operator of the absolute value (soft-thresholding) [Tibshirani, 1996], yielding $a_k^* = \text{sign}(u_k)(t|u_k| - \lambda)_+$. On full-activation set \mathcal{A} every coordinate is active with $a_k^* = \text{sign}(u_k)(t|u_k| - \lambda)$, and the k -th residual component is

$$tu_k - a_k^* = tu_k - \text{sign}(u_k)(t|u_k| - \lambda) = \lambda \text{sign}(u_k).$$

Summing over k and using orthonormality, $\|r(\mathbf{h})\|_2^2 = \lambda^2 \sum_{k=1}^{d_i} \text{sign}(u_k)^2 = d_i \lambda^2$ and the proof concludes with $\|r(\mathbf{h})\|_2 = \lambda \sqrt{d_i}$. \square

Proof of Theorem 6.

Proof. The point is that the residual $r(\mathbf{h})$ left by the basis decoder correlates with the off-basis direction $\tilde{\mathbf{d}}$ more strongly than λ , which is exactly the condition under which $\tilde{\mathbf{d}}$ would be activated. Write $\tilde{\mathbf{d}} = \sum_{k=1}^{d_i} c_k \mathbf{v}_k$ with $\|\mathbf{c}\|_2 = 1$ and at least two nonzero coordinates. On the full-activation set \mathcal{A} , Lemma 17 gives the residual $r(\mathbf{h}) = \lambda \sum_k \text{sign}(u_k) \mathbf{v}_k$, so orthonormality of the basis vectors yields

$$\tilde{\mathbf{d}}^\top r(\mathbf{h}) = \lambda \sum_{k=1}^{d_i} c_k \text{sign}(u_k),$$

which depends on \mathbf{u} only through the sign pattern $\boldsymbol{\sigma}(\mathbf{u}) = (\text{sign}(u_1), \dots, \text{sign}(u_{d_i}))$. For any $\boldsymbol{\sigma} \in \{-1, +1\}^{d_i}$, $\sum_k c_k \sigma_k \leq \sum_k |c_k| = \|\mathbf{c}\|_1$, with equality when $\sigma_k = \text{sign}(c_k)$ for every nonzero c_k . Since at least two coordinates of \mathbf{c} are nonzero, $\|\mathbf{c}\|_1 > \|\mathbf{c}\|_2 = 1$. On the aligned orthant $\mathcal{U}_{\mathbf{c}}$, the signs of \mathbf{u} match those of the nonzero coordinates of \mathbf{c} , giving $\tilde{\mathbf{d}}^\top r = \lambda \|\mathbf{c}\|_1 > \lambda$. \square

Proof of Proposition 7

Proof. We turn the certificate violation of Theorem 6 into a strictly lower risk by exhibiting a feasible code that activates the extra column. At $\mathbf{D} = [\mathbf{D}_{\text{basis}}, \tilde{\mathbf{d}}]$, the basis code $\tilde{\mathbf{a}}(\mathbf{h}) = (a_1^*, \dots, a_{d_i}^*, 0)$ is feasible with cost $L_{\text{basis}}(\mathbf{h})$ but violates the ℓ_1 stationarity (inactivity) condition $|\tilde{\mathbf{d}}^\top \mathbf{r}| \leq \lambda$ on $\mathcal{U}_{\mathbf{c}} \cap \mathcal{A}$ (Theorem 6).

We construct a strictly better feasible code. Keep the basis coordinates fixed and optimize over a_{d_i+1} . The cost becomes

$$L(a_{d_i+1}) = L_{\text{basis}}(\mathbf{h}) - a_{d_i+1}(\lambda \|\mathbf{c}\|_1 - \lambda) + \frac{a_{d_i+1}^2}{2}.$$

Minimizing over $a_{d_i+1} > 0$ yields $a_{d_i+1}^* = \lambda \|\mathbf{c}\|_1 - \lambda = \lambda(\|\mathbf{c}\|_1 - 1) > 0$ with

$$L(a_{d_i+1}^*) = L_{\text{basis}}(\mathbf{h}) - \frac{\lambda^2 (\|\mathbf{c}\|_1 - 1)^2}{2}.$$

Since the ℓ_1 -regularized optimum $L^*(\mathbf{h}; \mathbf{D})$ minimizes over all $d_i + 1$ coordinates jointly, we have $L^*(\mathbf{h}; \mathbf{D}) \leq L(a_{d_i+1}^*)$ and therefore

$$L_{\text{basis}}(\mathbf{h}) - L^*(\mathbf{h}; \mathbf{D}) \geq \frac{\lambda^2(\|\mathbf{c}\|_1 - 1)^2}{2} > 0$$

on $\mathcal{U}_c \cap \mathcal{A}$. For other points, feasibility of $\tilde{\mathbf{a}}(\mathbf{h})$ gives $L^* \leq L_{\text{basis}}$. The strict improvement on a set of positive measure and non-worsening elsewhere yield $R(\mathbf{D}_{\text{basis}}) - R(\mathbf{D}) > 0$. \square

Proof of Theorem 8

Proof. We promote the single-point certificate violation into a continuous descent path with rotating one extra decoder column toward the diagonal direction $\tilde{\mathbf{d}}$ leaves the risk flat until the column crosses the activation boundary, after which it strictly lowers the risk. Set $\tilde{\mathbf{d}} = \frac{1}{\sqrt{d_i}} \sum_{k=1}^{d_i} \mathbf{v}_k$, whose basis coordinates $\mathbf{c} = \frac{1}{\sqrt{d_i}} \mathbf{1}$ satisfy $\|\mathbf{c}\|_2 = 1$ and align with the all-positive orthant $\mathcal{U}^+ := \{\mathbf{u} \in \mathcal{A} : u_k > 0 \forall k\}$. Since $m > d_i$ and the ℓ_1 -regularized objective at \mathbf{D}_0 activates finitely many columns per input, there exists $j > d_i$ whose column \mathbf{d}_j is inactive on \mathcal{U}^+ , so that $|\mathbf{d}_j^\top r(\mathbf{h})| \leq \lambda$ there. Rotate column j along the geodesic

$$\mathbf{d}_j(\alpha) = \frac{\cos \alpha \mathbf{d}_j(0) + \sin \alpha \tilde{\mathbf{d}}}{\|\cos \alpha \mathbf{d}_j(0) + \sin \alpha \tilde{\mathbf{d}}\|_2}, \quad \alpha \geq 0.$$

Let $\mathbf{D}(\alpha)$ be \mathbf{D}_0 with column j replaced by $\mathbf{d}_j(\alpha)$. Since column j was inactive on $\mathcal{U}^+ \cap \mathcal{A}$, the optimal code at \mathbf{D}_0 for these inputs uses only the shared columns and remains feasible at $\mathbf{D}(\alpha)$ with the same cost. Any additional activation of $\mathbf{d}_j(\alpha)$ can only reduce the ℓ_1 -regularized objective, so

$$L^*(\mathbf{h}; \mathbf{D}(\alpha)) \leq L^*(\mathbf{h}; \mathbf{D}_0)$$

for all $\mathbf{h} = t\mathbf{u}$ and $\mathbf{u} \in \mathcal{U}^+$. Since $\|\mathbf{c}\|_1 = \sqrt{d_i}$ here, Theorem 6 gives $\tilde{\mathbf{d}}^\top r(\mathbf{h}) = \lambda\sqrt{d_i} > \lambda$. Writing $f(\alpha) = \mathbf{d}_j(\alpha)^\top r(\mathbf{h})/\lambda = \sqrt{d_i} (\mathbf{d}_j(\alpha)^\top \tilde{\mathbf{d}})$ and $\kappa = \mathbf{d}_j(0)^\top \tilde{\mathbf{d}}$, the inactivity bound gives $f(0) = \sqrt{d_i} \kappa \leq 1$, while $f(\alpha)$ goes to $\sqrt{d_i} > 1$ as $\mathbf{d}_j(\alpha)$ goes to $\tilde{\mathbf{d}}$. Since $\mathbf{d}_j(\alpha)^\top \tilde{\mathbf{d}}$ increases continuously from κ to 1 along the geodesic, f is continuous and increasing, and the boundary angle $\alpha_0 := \inf\{\alpha \geq 0 : f(\alpha) \geq 1\}$ is well defined with $f(\alpha_0) = 1$, $f < 1$ on $[0, \alpha_0)$, and $f > 1$ on $\alpha > \alpha_0$.

Keeping the basis code fixed and optimizing only the code a_j on the rotated column, the per-sample cost is $L(a_j) = L_{\text{basis}}(\mathbf{h}) - a_j (\mathbf{d}_j(\alpha)^\top r(\mathbf{h})) + \frac{1}{2} a_j^2$, minimized over $a_j \geq 0$ by $a_j^* = \lambda(f(\alpha) - 1)_+$ (Proposition 7), so

$$L^*(\mathbf{h}; \mathbf{D}(\alpha)) \leq L_{\text{basis}}(\mathbf{h}) - \frac{\lambda^2}{2} (f(\alpha) - 1)_+^2.$$

For $\alpha \in [0, \alpha_0]$ we have $f(\alpha) \leq 1$, the spare column stays inactive, and the reconstruction is unchanged on \mathcal{U}^+ , so combined with $L^*(\mathbf{h}; \mathbf{D}(\alpha)) \leq L^*(\mathbf{h}; \mathbf{D}_0)$ on $(\mathcal{U}^+)^c$ we get $R(\mathbf{D}(\alpha)) = R(\mathbf{D}_0)$. For $\alpha > \alpha_0$ the certificate is violated on \mathcal{U}^+ and the per-sample improvement is at least $\frac{\lambda^2}{2} (f(\alpha) - 1)^2 > 0$ there. On $(\mathcal{U}^+)^c$ the \mathbf{D}_0 optimal code on the shared columns is still feasible at $\mathbf{D}(\alpha)$, giving $L^*(\mathbf{h}; \mathbf{D}(\alpha)) \leq L^*(\mathbf{h}; \mathbf{D}_0)$. The orthant \mathcal{U}^+ carries mass $\Pr(\mathcal{U}^+) = 2^{-d_i}$, so integrating the per-sample improvement over it leaves

$$R(\mathbf{D}_0) - R(\mathbf{D}(\alpha)) \geq 2^{-(d_i+1)} \lambda^2 (f(\alpha) - 1)^2 > 0$$

for every $\alpha > \alpha_0$. Thus the path is flat on $[0, \alpha_0]$ and strictly descending afterward, exhibiting a continuous path from \mathbf{D}_0 to strictly lower risk. \square

A.2 Subspace-Aware Sparse Autoencoders

A.2.1 Proof of Proposition 10

Proof. Let $\mathbf{V}_i = [\mathbf{v}_1, \dots, \mathbf{v}_{d_i}]$ be an orthonormal basis of \mathcal{V}_i , so that $\mathcal{M}_i(t) \subseteq \mathcal{V}_i = \text{col}(\mathbf{V}_i)$. Because $r \geq d_i$, take the block $\mathbf{D}_{k^*} = [\mathbf{v}_1, \dots, \mathbf{v}_{d_i}, \mathbf{0}, \dots, \mathbf{0}] \in \mathbb{R}^{d \times r}$, whose first d_i columns carry the basis of \mathcal{V}_i and whose remaining $r - d_i$ columns vanish, and let $\{\mathbf{D}_k\}_{k=1}^K$ be any block decoder that contains it. Then $\mathcal{V}_i \subseteq \text{col}(\mathbf{D}_{k^*})$, and every $\mathbf{h} \in \mathcal{M}_i(t)$ satisfies $\mathbf{h} \in \mathcal{V}_i \subseteq \text{col}(\mathbf{D}_{k^*})$, so $\text{dist}(\mathbf{h}, \text{col}(\mathbf{D}_{k^*})) = 0$ and the supremum over the slice vanishes.

The reconstruction collapses to

$$\mathbf{D}_{k^*} a(\mathbf{h})_{k^*}(\mathbf{h}) = \mathbf{V}_i \mathbf{V}_i^\top \mathbf{h} = \mathbf{P}_{\mathcal{V}_i} \mathbf{h} = \mathbf{h},$$

the final equality holding because $\mathbf{h} \in \mathcal{V}_i$. A single active group therefore reconstructs every $\mathbf{h} \in \mathcal{M}_i(t)$ with zero error while co-activating the r columns of \mathbf{D}_{k^*} , which is Definition 2 with budget $k = r$. Since $r \geq d_i$, this lands in the regime where Theorem 4 gives $L_i^{(d_i)}(0) = d_i$ with no splitting. \square

A.2.2 Proof of Theorem 11

Proof. We show the SASA objective does the opposite of the standard SAE objective. Rather than rejecting the consolidated solution, it makes a single block carrying the whole feature the unique global minimizer. Fix the encoder \mathbf{E} and write $\mathbf{W}_k = \mathbf{D}_k \mathbf{E}_k$ for the per-block reconstruction map. The Top-1 gate partitions $\mathcal{M}_i(t)$ into the cells $\mathcal{C}_k = \{\mathbf{h} \in \mathcal{M}_i(t) : \|\mathbf{E}_k \mathbf{h}\|_2 > \|\mathbf{E}_{k'} \mathbf{h}\|_2 \ \forall k' \neq k\}$ with pairwise boundaries of measure zero, so the active block is constant almost everywhere on each cell and the objective separates as

$$R(\mathbf{E}, \mathbf{D}) = \sum_k \left[\text{tr}((\mathbf{I} - \mathbf{W}_k) \mathbf{M}_k (\mathbf{I} - \mathbf{W}_k)^\top) + \lambda_{\text{dim}} \|\mathbf{W}_k\|_* \right], \quad \mathbf{M}_k = \mathbb{E}[\mathbf{h} \mathbf{h}^\top \mathbb{1}\{\mathbf{h} \in \mathcal{C}_k\}],$$

and each \mathbf{W}_k is optimized against its own \mathbf{M}_k .

Since $\mathcal{M}_i(t) \subseteq \mathcal{V}_i$, we have $\text{col}(\mathbf{M}_k) \subseteq \mathcal{V}_i$. For an occupied cell, \mathcal{C}_k has positive measure on the sphere $\mathbb{S}^{d_i-1} \cap \mathcal{V}_i$ and so is not contained in any proper subset of \mathcal{V}_i , hence $\mathbf{M}_k \succ \mathbf{0}$ on \mathcal{V}_i with $\text{col}(\mathbf{M}_k) = \mathcal{V}_i$ and rank d_i . The trace term and the nuclear norm are unitarily invariant, so a minimizing \mathbf{W}_k is diagonal in the eigenbasis of \mathbf{M}_k , with any off-eigenbasis or out-of-range component strictly increasing the nuclear norm at no gain to the trace term. Writing $\mathbf{M}_k = \sum_j \mu_j \mathbf{q}_j \mathbf{q}_j^\top$ and $\mathbf{W}_k = \sum_j w_j \mathbf{q}_j \mathbf{q}_j^\top$, the per-cell cost reduces to $\sum_j [(1 - w_j)^2 \mu_j + \lambda_{\text{dim}} |w_j|]$, minimized over w_j by $w_j^* = (1 - \lambda_{\text{dim}}/2\mu_j)_+$ with optimal value $g(\mu_j)$, where

$$g(\mu) = \min \left\{ \mu, \lambda_{\text{dim}} - \frac{\lambda_{\text{dim}}^2}{4\mu} \right\}.$$

The function g is continuous and nondecreasing on $[0, \infty)$ with $g(0) = 0$ and is strictly concave on $(0, \infty)$, and the optimal cost of an occupied cell equals $\sum_j g(\mu_j) = \text{tr } g(\mathbf{M}_k)$.

A single block reconstructing the whole slice carries $\Sigma_i = \mathbb{E}_{\mathbf{h} \sim \mathcal{M}_i(t)}[\mathbf{h} \mathbf{h}^\top] = \frac{t^2}{d_i} \mathbf{P}_{\mathcal{V}_i}$, whose d_i eigenvalues equal t^2/d_i . It is precisely the assumed regime $\lambda_{\text{dim}} < t^2/d_i$ that places this common eigenvalue above the shrinkage threshold $\lambda_{\text{dim}}/2$, so $w_j^* > 0$ for all j and the single-block map attains $\text{col}(\mathbf{W}_{k^*}) = \mathcal{V}_i$ at effective rank d_i . Across any partition the occupied moments satisfy $\sum_k \mathbf{M}_k = \mathbb{E}[\mathbf{h} \mathbf{h}^\top] = \Sigma_i$, and the Rotfel'd trace inequality [Bourin, 2010] for the concave g with $g(0) = 0$ gives

$$\sum_k \text{tr } g(\mathbf{M}_k) \geq \text{tr } g\left(\sum_k \mathbf{M}_k\right) = \text{tr } g(\Sigma_i).$$

Strict concavity of g forces equality only when the occupied summands have mutually orthogonal ranges, yet every occupied \mathbf{M}_k has $\text{col}(\mathbf{M}_k) = \mathcal{V}_i$, so two active blocks share the range \mathcal{V}_i , leading to strict inequality. Every global minimizer thus activates a single block k^* .

The index k^* is free by symmetry of the objective across blocks. On the active block, g depends on $\mathbf{M}_{k^*} = \Sigma_i$ only through its spectrum, and the trace term is invariant under orthogonal maps of \mathcal{V}_i , so the minimizer is determined up to orthogonal rotation within \mathcal{V}_i .

Restricting R to the surviving block, the variational identity $\|\mathbf{D}_{k^*} \mathbf{E}_{k^*}\|_* = \min \frac{1}{2} (\|\mathbf{D}_{k^*}\|_F^2 + \|\mathbf{E}_{k^*}\|_F^2)$ recasts the objective as the regularized linear autoencoder $\|\mathbf{h} - \mathbf{D}_{k^*} \mathbf{E}_{k^*} \mathbf{h}\|_2^2 + \frac{\lambda_{\text{dim}}}{2} (\|\mathbf{D}_{k^*}\|_F^2 + \|\mathbf{E}_{k^*}\|_F^2)$, whose landscape has no spurious local minima and whose global minimizer aligns the decoder columns with the leading eigenvectors of Σ_i [Kunin et al., 2019, Theorem 4.2]. \square

A.3 Sample Complexity Efficiency

This section introduces some useful facts, which are key in the proof of Theorem 13 and Proposition 12 in the next section. To start with, we first revise the Matrix Bernstein inequality.

Theorem 18 (Theorem 1.4, Tropp [2012]). *Consider a finite sequence $\{\mathbf{X}_k\}$ of independent, random, self-adjoint matrices with dimension d . Assume that each random matrix satisfies*

$$\mathbb{E}[\mathbf{X}_k] = \mathbf{0} \quad \text{and} \quad \lambda_{\max}(\mathbf{X}_k) \leq R \quad \text{almost surely.}$$

Then, for all $t \geq 0$,

$$\mathbb{P} \left\{ \lambda_{\max} \left(\sum_k \mathbf{X}_k \right) \geq t \right\} \leq d \exp \left(\frac{-t^2}{2\sigma^2 + \frac{2}{3} R t} \right) \quad \text{where } \sigma^2 := \left\| \sum_k \mathbb{E}[(\mathbf{X}_k^2)] \right\|.$$

We now provide a matrix concentration inequality based on that as follows.

Lemma 19. Let $\mathbf{h}_1, \dots, \mathbf{h}_n \in \mathbb{R}^d$ be i.i.d. with $\|\mathbf{h}\|_2 = t$ and define $\boldsymbol{\Sigma} := \mathbb{E}_{\mathbf{h} \sim \mathcal{D}}[\mathbf{h}\mathbf{h}^\top]$, $\widehat{\boldsymbol{\Sigma}} := \frac{1}{n} \sum_{i=1}^n \mathbf{h}_i \mathbf{h}_i^\top$. Then for any $\delta \in (0, 1)$, with probability at least $1 - \delta$,

$$\|\widehat{\boldsymbol{\Sigma}} - \boldsymbol{\Sigma}\|_2 \leq 2t^2 \left(\frac{\log\left(\frac{2d}{\delta}\right)}{3n} + \frac{1}{n} \sqrt{\frac{\log^2\left(\frac{2d}{\delta}\right)}{9} + 2n \log\left(\frac{2d}{\delta}\right)} \right).$$

Proof. We apply the Matrix Bernstein inequality to the centered rank-one summands $\mathbf{h}_i \mathbf{h}_i^\top - \boldsymbol{\Sigma}$, for which the norm bound R and the variance proxy σ^2 follow directly from $\|\mathbf{h}\|_2 = t$. Define the centered self-adjoint random matrices

$$\mathbf{X}_i := \mathbf{h}_i \mathbf{h}_i^\top - \boldsymbol{\Sigma}, \quad \mathbf{S} := \sum_{i=1}^n \mathbf{X}_i,$$

so that $\mathbb{E}[\mathbf{X}_i] = \mathbf{0}$, $\widehat{\boldsymbol{\Sigma}} - \boldsymbol{\Sigma} = \frac{1}{n} \mathbf{S}$, and therefore $\|\widehat{\boldsymbol{\Sigma}} - \boldsymbol{\Sigma}\|_2 = \frac{1}{n} \|\mathbf{S}\|_2$. Let us first bound R and σ^2 . For R , note that based on Jensen's inequality, we have

$$\|\boldsymbol{\Sigma}\|_2 = \lambda_{\max}(\boldsymbol{\Sigma}) = \lambda_{\max}(\mathbb{E}[\mathbf{h}\mathbf{h}^\top]) \leq \mathbb{E}[\lambda_{\max}(\mathbf{h}\mathbf{h}^\top)] = \mathbb{E}[\|\mathbf{h}\mathbf{h}^\top\|_2] = t^2.$$

Hence, we have

$$\|\mathbf{X}_i\|_2 \leq \|\mathbf{h}_i \mathbf{h}_i^\top\|_2 + \|\boldsymbol{\Sigma}\|_2 \leq 2t^2$$

and we set $R = 2t^2$. Now for σ^2 , note that we have

$$\mathbb{E}[\mathbf{X}_i^2] \preceq 2\mathbb{E}[(\mathbf{h}\mathbf{h}^\top)^2] + 2\boldsymbol{\Sigma}^2 = 2\mathbb{E}[\|\mathbf{h}\|_2^2 \mathbf{h}\mathbf{h}^\top] + 2\boldsymbol{\Sigma}^2 \preceq 2t^2 \boldsymbol{\Sigma} + 2t^2 \boldsymbol{\Sigma} = 4t^2 \boldsymbol{\Sigma}.$$

So we have

$$\sigma^2 = \left\| \sum_{i=1}^n \mathbb{E}[\mathbf{X}_i^2] \right\|_2 \leq \sum_{i=1}^n 4t^2 \|\boldsymbol{\Sigma}\|_2 \leq 4nt^4.$$

Now note that we can write the spectral norm as the maximum over the largest positive eigenvalue and the negative of the smallest negative eigenvalue

$$\|\mathbf{S}\|_2 = \max\{\lambda_{\max}(\mathbf{S}), -\lambda_{\min}(\mathbf{S})\}$$

As we are looking to bound $\|\mathbf{S}\|_2$. By a simple union bound, then, we have

$$\mathbb{P}\{\|\mathbf{S}\|_2 \geq u\} \leq \mathbb{P}\{\lambda_{\max}(\mathbf{S}) \geq u\} + \mathbb{P}\{-\lambda_{\min}(\mathbf{S}) \geq u\}$$

which leads to

$$\mathbb{P}(\|\mathbf{S}\|_2 \geq u) \leq 2d \exp\left(-\frac{u^2}{2\sigma^2 + \frac{2}{3}Ru}\right).$$

To obtain a high-probability bound, it suffices to choose u so that

$$2d \exp\left(-\frac{u^2}{2\sigma^2 + \frac{2}{3}Ru}\right) \leq \delta.$$

Now, we have

$$\begin{aligned} \frac{u^2}{2\sigma^2 + \frac{2}{3}Ru} &\geq \log\left(\frac{2d}{\delta}\right) \\ \implies u^2 - \frac{2R}{3} \log\left(\frac{2d}{\delta}\right) u - 2 \log\left(\frac{2d}{\delta}\right) \sigma^2 &\geq 0 \end{aligned}$$

which is quadratic in u and is satisfied when

$$u \geq \frac{R}{3} \log\left(\frac{2d}{\delta}\right) + \sqrt{\frac{R^2}{9} \log^2\left(\frac{2d}{\delta}\right) + 2\sigma^2 \log\left(\frac{2d}{\delta}\right)}$$

which leads to that with probability $1 - \delta$,

$$\|\mathbf{S}\|_2 \leq \frac{R}{3} \log\left(\frac{2d}{\delta}\right) + \sqrt{\frac{R^2}{9} \log^2\left(\frac{2d}{\delta}\right) + 2\sigma^2 \log\left(\frac{2d}{\delta}\right)}.$$

Finally, substituting $\widehat{\Sigma} - \Sigma = \frac{1}{n}\mathbf{S}$, $R = 2t^2$, and $\sigma^2 \leq 4nt^4$, we have that with probability $1 - \delta$

$$\begin{aligned} \|\mathbf{S}\|_2 &\leq \frac{R}{3} \log\left(\frac{2d}{\delta}\right) + \sqrt{\frac{R^2}{9} \log^2\left(\frac{2d}{\delta}\right) + 2\sigma^2 \log\left(\frac{2d}{\delta}\right)} \\ \implies \|\widehat{\Sigma} - \Sigma\|_2 &\leq \frac{2t^2}{3n} \log\left(\frac{2d}{\delta}\right) + \frac{1}{n} \sqrt{\frac{4t^4}{9} \log^2\left(\frac{2d}{\delta}\right) + 8nt^4 \log\left(\frac{2d}{\delta}\right)} \\ \implies \|\widehat{\Sigma} - \Sigma\|_2 &\leq \frac{2t^2}{3n} \log\left(\frac{2d}{\delta}\right) + \frac{2t^2}{n} \sqrt{\frac{\log^2\left(\frac{2d}{\delta}\right)}{9} + 2n \log\left(\frac{2d}{\delta}\right)} \\ &= 2t^2 \left(\frac{\log\left(\frac{2d}{\delta}\right)}{3n} + \frac{1}{n} \sqrt{\frac{\log^2\left(\frac{2d}{\delta}\right)}{9} + 2n \log\left(\frac{2d}{\delta}\right)} \right). \end{aligned}$$

□

Lemma 19 provides a high-probability norm control of the perturbation $\widehat{\Sigma} - \Sigma$. Next, we restate one variant of Davis–Kahan Theorems.

Theorem 20 (Theorem 1, Yu et al. [2014]). *Let $\Sigma, \widehat{\Sigma} \in \mathbb{R}^{p \times p}$ be symmetric, with eigenvalues $\lambda_1 \geq \dots \geq \lambda_p$ and $\widehat{\lambda}_1 \geq \dots \geq \widehat{\lambda}_p$ respectively. Fix $1 \leq r \leq s \leq p$, let $d = s - r + 1$, and let $\mathbf{V} = (\mathbf{v}_r, \mathbf{v}_{r+1}, \dots, \mathbf{v}_s) \in \mathbb{R}^{p \times d}$ and $\widehat{\mathbf{V}} = (\widehat{\mathbf{v}}_r, \widehat{\mathbf{v}}_{r+1}, \dots, \widehat{\mathbf{v}}_s) \in \mathbb{R}^{p \times d}$ have orthonormal columns satisfying $\Sigma \mathbf{v}_j = \lambda_j \mathbf{v}_j$ and $\widehat{\Sigma} \widehat{\mathbf{v}}_j = \widehat{\lambda}_j \widehat{\mathbf{v}}_j$ for $j = r, r+1, \dots, s$. Write $\delta = \inf\{|\widehat{\lambda} - \lambda| : \lambda \in [\lambda_s, \lambda_r], \widehat{\lambda} \in (-\infty, \widehat{\lambda}_{s+1}] \cup [\widehat{\lambda}_{r-1}, \infty)\}$, where we define $\widehat{\lambda}_0 = -\infty$ and $\widehat{\lambda}_{p+1} = \infty$, and assume that $\delta > 0$. Then*

$$\|\sin \Theta(\widehat{\mathbf{V}}, \mathbf{V})\|_2 \leq \frac{\|\widehat{\Sigma} - \Sigma\|_2}{\delta}.$$

The following lemma now turns the matrix perturbation bound in Lemma 19 into a bound on the operator norm of the difference of orthogonal projectors.

Lemma 21 (Davis–Kahan projector bound). *Let $\Sigma, \widehat{\Sigma} \in \mathbb{R}^{d \times d}$ be symmetric. Fix an integer $d_i < d$, and let \mathcal{V} and $\widehat{\mathcal{V}}$ denote the top- d_i eigenspaces of Σ and $\widehat{\Sigma}$, respectively. Write the eigenvalues of Σ as $\lambda_1 \geq \lambda_2 \geq \dots \geq \lambda_d$, and define the population eigengap $\Delta := \lambda_{d_i} - \lambda_{d_i+1} > 0$. If*

$$\|\widehat{\Sigma} - \Sigma\|_2 \leq \frac{\Delta}{2},$$

then

$$\|\mathbf{P}_{\widehat{\mathcal{V}}} - \mathbf{P}_{\mathcal{V}}\|_2 \leq \frac{2}{\Delta} \|\widehat{\Sigma} - \Sigma\|_2.$$

Proof. The bound converts a perturbation of the second-moment matrix into a perturbation of its top- d_i eigenspace, measured by the operator norm of the gap between the two projectors. Choose matrices $\mathbf{V}, \widehat{\mathbf{V}} \in \mathbb{R}^{d \times d_i}$ with orthonormal columns spanning \mathcal{V} and $\widehat{\mathcal{V}}$, respectively, so that $\mathbf{P}_{\mathcal{V}} = \mathbf{V}\mathbf{V}^\top$ and $\mathbf{P}_{\widehat{\mathcal{V}}} = \widehat{\mathbf{V}}\widehat{\mathbf{V}}^\top$. It is shown in Corollary 2.13 of Knyazev et al. [2010] that

$$\|\mathbf{P}_{\widehat{\mathcal{V}}} - \mathbf{P}_{\mathcal{V}}\|_2 = \max_{j \in [d_i]} \sin \theta_j = \|\sin \Theta(\widehat{\mathbf{V}}, \mathbf{V})\|_2, \quad (10)$$

where $\sin \Theta(\widehat{\mathbf{V}}, \mathbf{V})$ is the diagonal matrix with entries $\sin \theta_j$ corresponding to the sine of the j -th principal angle between \mathbf{V} and $\widehat{\mathbf{V}}$. Using Theorem 20 and the fact that $\delta = \lambda_{d_i} - \widehat{\lambda}_{d_i+1}$, we have

$$\|\sin \Theta(\widehat{\mathbf{V}}, \mathbf{V})\|_2 \leq \frac{\|\widehat{\Sigma} - \Sigma\|_2}{\lambda_{d_i} - \widehat{\lambda}_{d_i+1}}, \quad (11)$$

Using Corollary 6.3.4 of Horn and Johnson [1985], we have $\widehat{\lambda}_{d_i+1} \leq \lambda_{d_i+1} + \|\widehat{\Sigma} - \Sigma\|_2$, so

$$\lambda_{d_i} - \widehat{\lambda}_{d_i+1} \geq \lambda_{d_i} - \lambda_{d_i+1} - \|\widehat{\Sigma} - \Sigma\|_2 = \Delta - \|\widehat{\Sigma} - \Sigma\|_2 \geq \frac{\Delta}{2},$$

where the last step uses the assumption $\|\widehat{\Sigma} - \Sigma\|_2 \leq \frac{\Delta}{2}$. Substituting this into (11) yields

$$\|\sin \Theta(\widehat{\mathbf{V}}, \mathbf{V})\|_2 \leq \frac{2}{\Delta} \|\widehat{\Sigma} - \Sigma\|_2.$$

Finally, combining with (10) gives

$$\|\mathbf{P}_{\widehat{\mathcal{V}}} - \mathbf{P}_{\mathcal{V}}\|_2 \leq \frac{2}{\Delta} \|\widehat{\Sigma} - \Sigma\|_2,$$

which concludes the proof. \square

Now using these, we are ready to prove Theorem 13.

A.3.1 Proof of Theorem 13

Proof. By Theorem 11 the SASA estimator on the slice is the top- d_i eigenspace of the empirical second moment, so recovering the feature reduces to principal subspace estimation. We bound its sample complexity by combining the concentration of Lemma 19 with the Davis–Kahan bound of Lemma 21. Recall that $\mathcal{M}_i(t)$ is the radius- t slice inside \mathcal{V}_i . Define the population covariance on the slice

$$\Sigma_i := \mathbb{E}_{\mathbf{h} \sim \mathcal{M}_i(t)} [\mathbf{h}\mathbf{h}^\top],$$

with $\|\mathbf{h}\|_2 = t$. Note that $\mathcal{M}_i(t) \subseteq \mathcal{V}_i$, so Σ_i has range contained in \mathcal{V}_i and therefore $\lambda_{d_i+1}(\Sigma_i) = 0$. Moreover, because the slice is the uniform sphere of radius t inside \mathcal{V}_i , the population covariance takes the isotropic form $\Sigma_i = \frac{t^2}{d_i} \mathbf{P}_{\mathcal{V}_i}$. Hence the top- d_i eigenspace of Σ_i is exactly \mathcal{V}_i , and the population eigengap equals

$$\Delta := \lambda_{d_i}(\Sigma_i) - \lambda_{d_i+1}(\Sigma_i) = \frac{t^2}{d_i}.$$

Let $\widehat{\Sigma}_i = \frac{1}{n} \sum_{j=1}^n \mathbf{h}_j \mathbf{h}_j^\top$ and let $\widehat{\mathcal{V}}_i$ be the top- d_i eigenspace of $\widehat{\Sigma}_i$. By Lemma 19, with probability at least $1 - \delta$,

$$\|\widehat{\Sigma}_i - \Sigma_i\|_2 \leq 2t^2 \left(\frac{\log\left(\frac{2d}{\delta}\right)}{3n} + \frac{1}{n} \sqrt{\frac{\log^2\left(\frac{2d}{\delta}\right)}{9} + 2n \log\left(\frac{2d}{\delta}\right)} \right).$$

Using $\sqrt{a+b} \leq \sqrt{a} + \sqrt{b}$ with $a = \frac{\log^2\left(\frac{2d}{\delta}\right)}{9}$ and $b = 2n \log\left(\frac{2d}{\delta}\right)$ gives

$$\|\widehat{\Sigma}_i - \Sigma_i\|_2 \leq 2t^2 \left(\frac{\log\left(\frac{2d}{\delta}\right)}{3n} + \frac{1}{n} \left(\frac{\log\left(\frac{2d}{\delta}\right)}{3} + \sqrt{2n \log\left(\frac{2d}{\delta}\right)} \right) \right) = \frac{4t^2 \log\left(\frac{2d}{\delta}\right)}{3n} + 2t^2 \sqrt{\frac{2 \log\left(\frac{2d}{\delta}\right)}{n}}.$$

We need to make sure the RHS is $\leq \frac{t\varepsilon}{2d_i}$. It suffices to require each term on the right-hand side to be at most $\frac{t\varepsilon}{4d_i}$.

$$\frac{4t^2 \log\left(\frac{2d}{\delta}\right)}{3n} \leq \frac{t\varepsilon}{4d_i}, \quad 2t^2 \sqrt{\frac{2 \log\left(\frac{2d}{\delta}\right)}{n}} \leq \frac{t\varepsilon}{4d_i}.$$

These conditions are equivalent to

$$n \geq \frac{16}{3} d_i t \frac{\log\left(\frac{2d}{\delta}\right)}{\varepsilon}, \quad n \geq 128 d_i^2 \frac{t^2 \log\left(\frac{2d}{\delta}\right)}{\varepsilon^2}.$$

Now if

$$n \geq 128 d_i^2 \frac{t^2 \log\left(\frac{2d}{\delta}\right)}{\varepsilon^2},$$

it satisfies both inequalities. Then

$$\|\widehat{\Sigma}_i - \Sigma_i\|_2 \leq \frac{t\varepsilon}{2d_i} = \frac{\Delta}{2} \cdot \frac{\varepsilon}{t} \leq \frac{\Delta}{2}.$$

Therefore Lemma 21 applies and yields

$$\|\mathbf{P}_{\widehat{\mathcal{V}}_i} - \mathbf{P}_{\mathcal{V}_i}\|_2 \leq \frac{2}{\Delta} \|\widehat{\Sigma}_i - \Sigma_i\|_2 \leq \frac{2}{\frac{t^2}{d_i}} \cdot \frac{t\varepsilon}{2d_i} = \frac{\varepsilon}{t}.$$

Finally, for any $\mathbf{h} \in \mathcal{M}_i(t)$ with $\|\mathbf{h}\|_2 = t$, we have $\mathbf{h} \in \mathcal{V}_i$ and thus

$$\text{dist}(\mathbf{h}, \widehat{\mathcal{V}}_i) = \|(I - \mathbf{P}_{\widehat{\mathcal{V}}_i})\mathbf{h}\|_2 = \|(\mathbf{P}_{\mathcal{V}_i} - \mathbf{P}_{\widehat{\mathcal{V}}_i})\mathbf{h}\|_2 \leq \|\mathbf{P}_{\widehat{\mathcal{V}}_i} - \mathbf{P}_{\mathcal{V}_i}\|_2 \|\mathbf{h}\|_2 \leq \frac{\varepsilon}{t} \cdot t = \varepsilon.$$

Taking the supremum over $\mathbf{h} \in \mathcal{M}_i(t)$ with $\|\mathbf{h}\|_2 = t$ completes the proof. \square

A.3.2 Proof of Proposition 12

Proof. For a standard SAE in the line-covering regime, each of the N decoder directions must receive at least one routed sample to be trained at all, so the number of activations required is governed by how many draws are needed to hit every index. Under the assumption of balanced routing, the problem of ensuring every direction receives at least one sample is equivalent to the Coupon Collector’s Problem with N distinct coupons (directions) and n trials (samples). Let T be the number of samples required to ensure $C_j \geq 1$ for all $j \in [N]$. According to [Doumas and Papanicolaou \[2015\]](#) Equation 1.3, the random variable T follows a Gumbel limit distribution:

$$\lim_{N \rightarrow \infty} \mathbb{P}\left(\frac{T - N \ln N}{N} \leq y\right) = \exp(-e^{-y}).$$

We seek to bound the probability of the failure event $\{\exists j \in [N] : C_j = 0\}$, which is equivalent to $\{T > n\}$. Let $y = \log(\frac{1}{\delta})$. Substituting into the limit expression, the threshold for sample size becomes $n^* \approx N(\ln N + \log(\frac{1}{\delta}))$. At this threshold, the probability of successfully training all directions is

$$\mathbb{P}(T \leq n^*) = \exp(-e^{-\log(\frac{1}{\delta})}) = \exp(-\delta).$$

Using the inequality $e^{-x} \geq 1 - x$, we have $\mathbb{P}(T \leq n^*) \geq 1 - \delta$. Consequently, the probability of failure at this threshold is $\mathbb{P}(T > n^*) \leq \delta$. Since $\mathbb{P}(T > n)$ is a strictly decreasing function of n , for any sample size $n < N(\ln N + \log(\frac{1}{\delta}))$, the probability of failure strictly exceeds δ . \square

B Training of SASA

This section provides details on SASA training.

B.1 LLMs and Layers

We train on residual-stream activations from two pretrained LLMs: (i) GPT-2 Small ($d = 768$) and (ii) Mistral-7B-v0.1 ($d = 4096$). For each model, we cache activations at a single mid-layer residual-stream hook of the form `blocks.l.hook_resid_pre`. Concretely, we use `blocks.7.hook_resid_pre` for GPT-2 and `blocks.8.hook_resid_pre` for Mistral. Unless stated otherwise, each token position yields one training example h_t .

B.2 Data

Corpora. GPT-2 SAEs/SASA are trained on OpenWebText [[Gokaslan et al., 2019](#)]. Mistral SAEs/SASA are trained on Pile [[Gao et al., 2020](#)].

Context length and token budgets. We train on sequences of a fixed context length per model. For GPT-2 we use context length 128 and a training budget of 150M tokens. For Mistral we use context length 512 and a training budget of 500M tokens. Tokenization uses each model’s native tokenizer. We stream data and do not update the LLM parameters.

B.3 Optimization and Hyperparameters

Implementations. We train SASA using SAELens with a custom `TrainingSAE` class that implements group-structured latents and Top- s gating over group norms.

Architecture hyperparameters. We parameterize SASA by (K, r, s) . Given a target width m and target scalar sparsity ℓ_0 , we choose a rank r and set $K = m/r$ and $s = \ell_0/r$. In our main GPT-2 runs we use $(K, r, s) = (2048, 6, 10)$, yielding $m = 12288$ and $\ell_0 = 60$. In our Mistral runs we use $(K, r, s) = (4096, 8, 10)$, yielding $m = 32768$ and $\ell_0 = 80$. We use $\lambda_{\text{aux}} = 1$. We set $s_{\text{aux}} = 512$ for GPT-2 runs and $s_{\text{aux}} = 256$ for Mistral runs.

Optimizer and schedule. We use AdamW with $(\beta_1, \beta_2) = (0.9, 0.999)$, learning rate 2×10^{-4} , and weight decay 10^{-3} . We linearly warm up for 1000 steps and then linearly decay the learning rate over one-fifth of the training. The token batch size is 4096 tokens, and we buffer 128 such batches for efficient streaming.

Activation normalization and biases. Inputs are normalized using `layer_norm` activation normalization.

C Algorithm Details of SASA

C.1 Auxiliary Loss

Top- s gating can leave some groups rarely active [Gao et al., 2024]. Let π_k denote a running estimate of the activation frequency of group k . We define the dead set

$$\mathcal{K}_{\text{dead}} = \{k \in [K] : \pi_k \leq \nu\},$$

where $\nu = 10^{-4}$ is the deadness threshold over a window of 1000 tokens.

For each \mathbf{h} , define the residual

$$r(\mathbf{h}) = \mathbf{h} - \mathbf{D}a(\mathbf{h}),$$

and treat $r(\mathbf{h})$ as a frozen target (i.e., gradients do not flow through \mathbf{r}). For dead groups, compute residual pre-activations

$$\tilde{p}_k(\mathbf{h}) = \mathbf{E}_k r(\mathbf{h}), \quad k \in \mathcal{K}_{\text{dead}}.$$

We then select s_{aux} dead groups with the largest residual energy.

$$\tilde{\mathcal{T}}_{s_{\text{aux}}}(\mathbf{h}) \in \arg \max_{T \subset \mathcal{K}_{\text{dead}}, |T|=s_{\text{aux}}} \sum_{k \in T} \|\tilde{p}_k(\mathbf{h})\|_2^2,$$

and define auxiliary activations

$$\tilde{a}_k(\mathbf{h}) = \begin{cases} \tilde{p}_k(\mathbf{h}), & k \in \tilde{\mathcal{T}}_{s_{\text{aux}}}(\mathbf{h}), \\ \mathbf{0}, & \text{o.w.} \end{cases}.$$

The auxiliary reconstruction uses only dead groups and targets the frozen residual.

$$\mathcal{L}_{\text{aux}}(\mathbf{h}) = \|r(\mathbf{h}) - \mathbf{D}\tilde{a}(\mathbf{h})\|_2^2. \quad (12)$$

C.2 Pseudo-code of SASA

In this section, we present the pseudo-code for both the training and inference procedures of the proposed SASA in Algorithm 1 and Algorithm 2, respectively.

C.2.1 Training

Below is the pseudocode for training SASA on a minibatch of hidden states. In addition to the reconstruction loss, we add the auxiliary loss (see Appendix C.1) and the nuclear-norm regularization loss.

C.2.2 Inference

Below is the pseudo-code for inference and interpretation using SASA. Unlike standard SAEs, for which a single latent value represents the *intensity* of the feature, in SASA, the respective group norm serves for that.

Algorithm 1 SASA training step

Input: minibatch $\{\mathbf{h}^{(j)}\}_{j=1}^B$, parameters $\{\mathbf{E}_k, \mathbf{D}_k\}_{k=1}^K$

Hyperparameters: $s, s_{\text{aux}}, \lambda_{\text{aux}}, \lambda_{\text{dim}}$

$J \leftarrow 0$.

for $j = 1$ **to** B **do**

$\mathbf{h} \leftarrow \mathbf{h}^{(j)}$, $p(\mathbf{h}) \leftarrow \mathbf{E}\mathbf{h}$ with blocks $p_k(\mathbf{h}) = \mathbf{E}_k\mathbf{h}$

$\mathcal{T}_s(\mathbf{h}) \in \arg \max_{T \subset [K], |T|=s} \sum_{k \in T} \|p_k(\mathbf{h})\|_2$

$a_k(\mathbf{h}) \leftarrow p_k(\mathbf{h})$ if $k \in \mathcal{T}_s(\mathbf{h})$, else $a_k(\mathbf{h}) \leftarrow \mathbf{0}$

$\mathcal{L}_{\text{aux}}(\mathbf{h}) \leftarrow 0$

$\mathcal{K}_{\text{dead}} \leftarrow$ set of dead neurons

if $\mathcal{K}_{\text{dead}} \neq \emptyset$ **then**

$r(\mathbf{h}) \leftarrow \mathbf{h} - \mathbf{D}a(\mathbf{h})$

for each $k \in \mathcal{K}_{\text{dead}}$ **do**

$\tilde{p}_k(\mathbf{h}) \leftarrow \mathbf{E}_k r(\mathbf{h})$

end for

$\tilde{\mathcal{T}}_{s_{\text{aux}}}(\mathbf{h}) \in \arg \max_{T \subset \mathcal{K}_{\text{dead}}, |T|=s_{\text{aux}}} \sum_{k \in T} \|\tilde{p}_k(\mathbf{h})\|_2^2$

$\tilde{a}_k(\mathbf{h}) \leftarrow \tilde{p}_k(\mathbf{h})$ if $k \in \tilde{\mathcal{T}}_{s_{\text{aux}}}(\mathbf{h})$, else $\tilde{a}_k(\mathbf{h}) \leftarrow \mathbf{0}$

$\mathcal{L}_{\text{aux}}(\mathbf{h}) \leftarrow \|r(\mathbf{h}) - \mathbf{D}\tilde{a}(\mathbf{h})\|_2^2$

end if

$J \leftarrow J + \|\mathbf{h} - \mathbf{D}a(\mathbf{h})\|_2^2 + \lambda_{\text{aux}}\mathcal{L}_{\text{aux}}(\mathbf{h})$

end for

$J \leftarrow \frac{1}{B}J + \lambda_{\text{dim}} \sum_{k=1}^K \|\mathbf{D}_k \mathbf{E}_k\|_*$

Update (\mathbf{E}, \mathbf{D}) to minimize J .

Algorithm 2 SASA reconstruction inference

Input: LLM activation \mathbf{h} , trained parameters $\{\mathbf{E}_k, \mathbf{D}_k\}_{k=1}^K$, sparsity level s

for $k = 1$ **to** K **do**

$p_k(\mathbf{h}) \leftarrow \mathbf{E}_k\mathbf{h}$

end for

$\mathcal{T}_s(\mathbf{h}) \in \arg \max_{T \subset [K], |T|=s} \sum_{k \in T} \|p_k(\mathbf{h})\|_2$

for $k = 1$ **to** K **do**

$a_k(\mathbf{h}) \leftarrow p_k(\mathbf{h})$ if $k \in \mathcal{T}_s(\mathbf{h})$, else $a_k(\mathbf{h}) \leftarrow \mathbf{0}$

end for

Output: Reconstruction $\mathbf{D}a(\mathbf{h}) = \sum_{k=1}^K \mathbf{D}_k a_k(\mathbf{h})$, sparse codes $\{a_k(\mathbf{h})\}_{k=1}^K$, active set $\mathcal{T}_s(\mathbf{h})$

Feature intensity: For feature k , intensity is $\|a_k(\mathbf{h})\|_2$.

D Low-dimensional Structure Validation

This appendix collects experimental results on the validation of the low-dimensional subspace assumption.

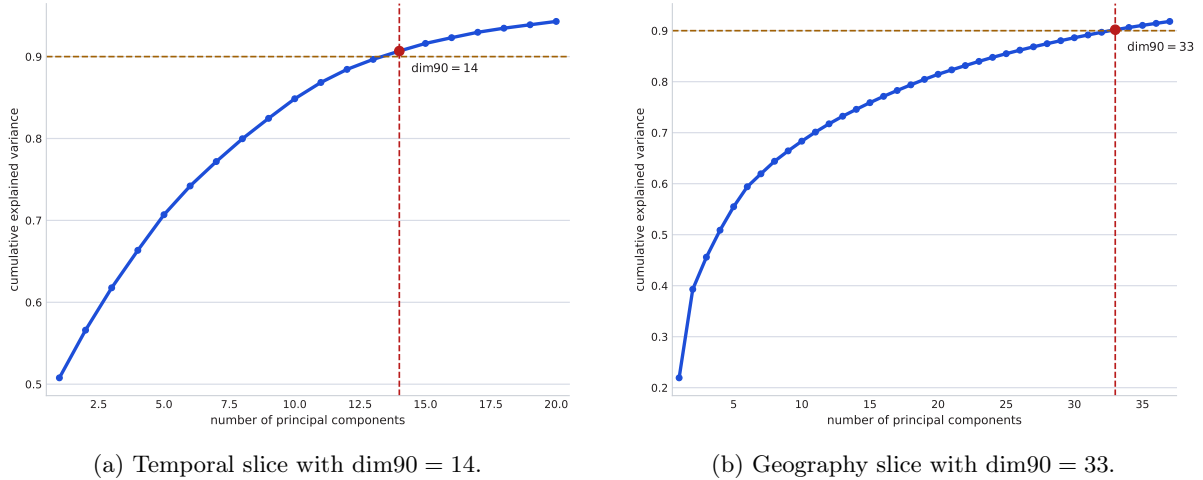


Figure 4: **Intrinsic dimensionality in raw GPT-2 activations** (no SAE involved). PCA on controlled concept prompts confirms compact subspaces within the 768-dimensional activation space.

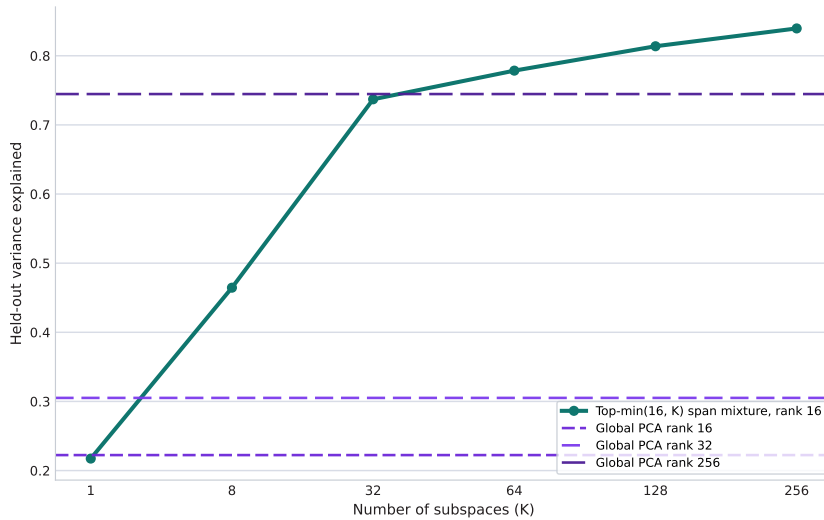


Figure 5: **Mixture-of-subspaces reconstruction in raw GPT-2 activations**. Rank-16 local PCA at $K = 256$ clusters captures 83.95% of held-out variance, exceeding global PCA at rank 256 (74.46%).

Section 7.3 briefly summarizes the low-dimensional structure validation. Here we provide the full figures and methodology. We apply PCA directly to GPT-2 layer-7 activations on controlled concept prompts (Appendix F.2), without any SAE decoder. Figure 4 shows that the temporal slice has $\text{dim90} = 14$ and the geography slice has $\text{dim90} = 33$, both out of 768 total dimensions.

To test whether the low-dimensional structure extends beyond individual concepts, we fit a mixture-of-subspaces model on raw OpenWebText activations. We sample 120k/30k train/test activations from layer 7, run K -means, and fit local rank-16 PCA within each cluster. Each test activation is reconstructed by projection onto the span of up to 16 selected local subspaces. At $K = 256$ clusters, this model captures 83.95% of held-out variance versus 74.46% for global PCA at rank 256 (Figure 5), confirming that raw GPT-2 activations are better described by a mixture of low-dimensional local subspaces than by a single global one.

E Clustering Standard SAEs

Here in this section, we analyze the clusters of decoder atoms. We first cluster all the vectors in the SAE decoder. For GPT-2, we perform spectral clustering, and for Mistral-7B, we treat each vector as a node and compute the pairwise cosine similarity matrix of decoder vectors as the graph’s adjacency matrix, then prune edges with similarity less than 0.5. Clusters will be the connected components of the remaining graph.

We then select clusters with size greater than 3, compute the PCA dimensionality that captures at least 80% of the cluster’s variance, and compare it with the cluster size. Figure 6 and Figure 7 show the result. As shown in these figures, the cluster size over PCA ratio indicates that we actually need fewer vectors to capture most of the variance, suggesting that many of these clusters have collinear coverage directions and can be expressed with fewer atoms. This shows the consequence of feature splitting on *wasting SAE’s capability* to devote more atoms than needed to discover a feature.

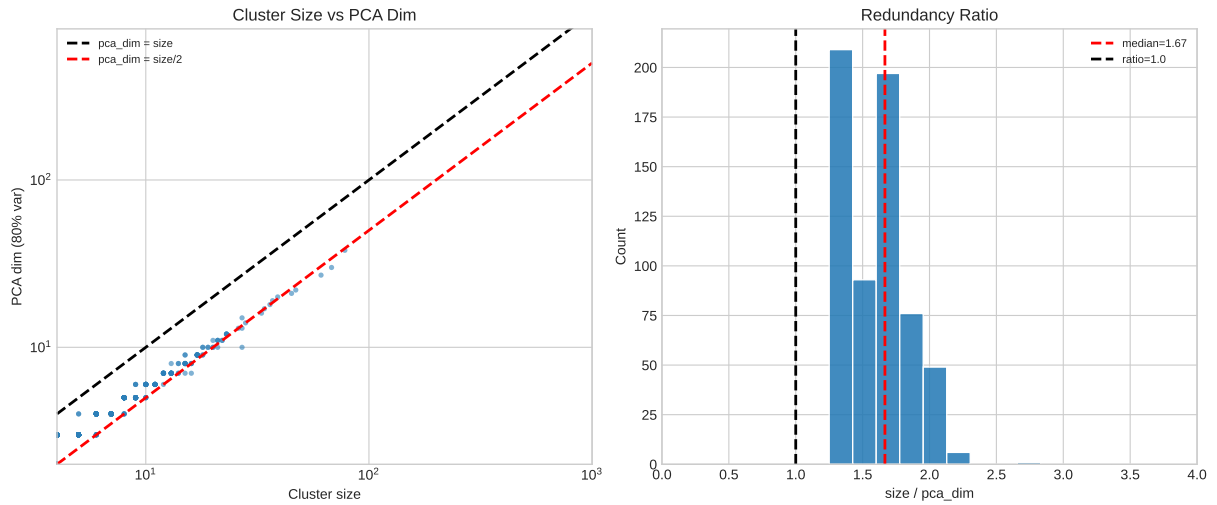


Figure 6: **Redundancy Ratio of Mistral-7B SAE Decoder Clusters.** The left panel shows cluster size vs PCA dimension (capturing 80% variance). The right panel shows a histogram of redundancy ratios. The median ratio of 1.67 suggests features are often split across multiple collinear vectors, indicating inefficiency.

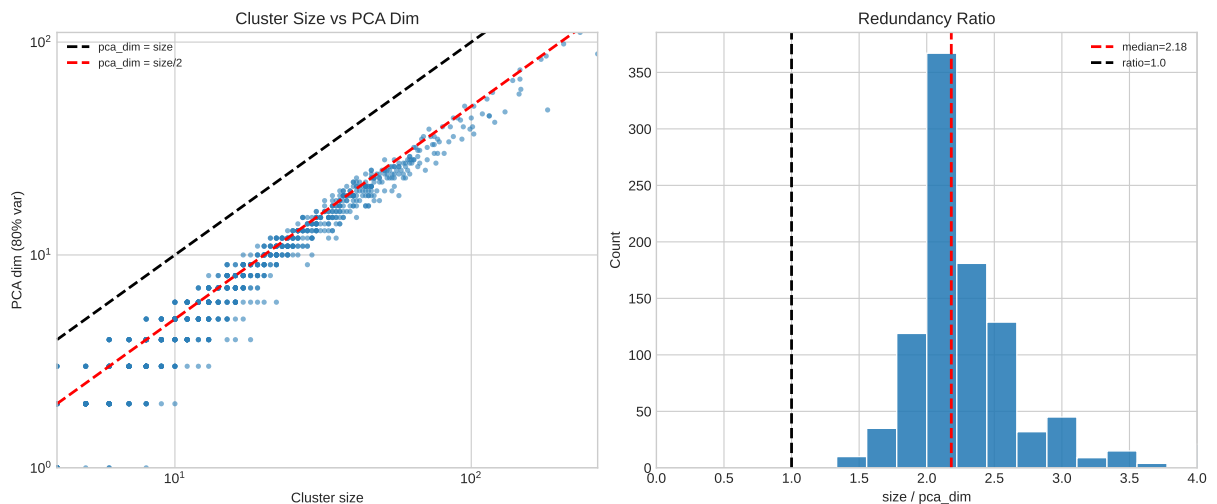


Figure 7: **Redundancy Ratio of GPT-2 SAE Decoder Clusters.** The median redundancy ratio of 2.18 highlights significant feature splitting, where standard SAEs use excess vectors to represent lower-dimensional subspaces, wasting model capacity.

F Additional Experiments Details

F.1 Feature Absorption Benchmark Details

We evaluate feature absorption using the first-letter absorption benchmark from Chanin et al. [2025]. Prompts follow the in-context spelling template `{word} has the first letter:` with up to 10 in-context examples drawn from alphabetic tokens. We record residual-stream activations at the queried-word position.

Detecting splitting and selecting main features. For each letter $\ell \in \{a, \dots, z\}$, we train k -sparse logistic probes on SAE activations $a(\mathbf{h})(\mathbf{h}) \in \mathbb{R}^m$ to predict whether the correct answer is ℓ , for $k = 1, \dots, 10$. Let $F1_\ell^{(k)}$ denote the best F1 score at sparsity k , and let $\mathcal{S}_\ell^{(k)} \subset [m]$ be the corresponding selected feature indices. We detect splitting when

$$F1_\ell^{(k)} - F1_\ell^{(k-1)} \geq \delta_{F1}, \quad (13)$$

with $\delta_{F1} = 0.03$, and define the selected set $\mathcal{S}_\ell := \mathcal{S}_\ell^{(k)}$ as the letter’s *main* features (larger k indicates more splitting).

Absorption metrics. Let $\mathbf{p}_\ell \in \mathbb{R}^d$ be a unit-normalized ground-truth residual-stream probe direction for letter ℓ , and let $\mathbf{d}_j \in \mathbb{R}^d$ be the unit-normalized decoder direction of SAE feature j . We decompose the probe-aligned projection across features via

$$s_{\ell,j}(\mathbf{h}) := [a(\mathbf{h})]_j \cos(\mathbf{d}_j, \mathbf{p}_\ell), \quad S_\ell(\mathbf{h}) := \sum_{j: s_{\ell,j}(\mathbf{h}) > 0} s_{\ell,j}(\mathbf{h}). \quad (14)$$

We evaluate on *false negatives* for letter ℓ , the token instances where the ground-truth probe predicts positive but the k -sparse SAE predictor (using \mathcal{S}_ℓ) predicts negative.

Fix thresholds $\tau_{\text{align}} = 0.1$, $\tau_{\text{frac}} = 0.4$, and $K_{\text{max}} = 3$. For a false-negative instance with state \mathbf{h} , define the candidate absorbing features

$$\mathcal{J}_\ell(\mathbf{h}) := \{j \notin \mathcal{S}_\ell : \cos(\mathbf{d}_j, \mathbf{p}_\ell) \geq \tau_{\text{align}}\}, \quad (15)$$

and let $\mathcal{A}_\ell(\mathbf{h}) \subseteq \mathcal{J}_\ell(\mathbf{h})$ be the set of up to K_{max} indices with largest $s_{\ell,j}(\mathbf{h})$. The *absorption fraction* is

$$\alpha_\ell(\mathbf{h}) := \frac{\sum_{j \in \mathcal{A}_\ell(\mathbf{h})} s_{\ell,j}(\mathbf{h})}{S_\ell(\mathbf{h})}, \quad (16)$$

and we count absorption when $\alpha_\ell(\mathbf{h}) \geq \tau_{\text{frac}}$. We report *Mean fraction absorption* by averaging $\alpha_\ell(\mathbf{h})$ over false negatives and then averaging over eligible letters.

Full absorption. Full absorption is the stricter event where no main feature fires and a *single* probe-aligned feature explains at least a τ_{frac} fraction of $S_\ell(\mathbf{h})$. With $\tau_{\text{full}} = 0.025$, define

$$\beta_\ell(\mathbf{h}) := \mathbb{I}[\forall j \in \mathcal{S}_\ell, [a(\mathbf{h})(\mathbf{h})]_j = 0] \cdot \mathbb{I}\left[\max_{j: \cos(\mathbf{d}_j, \mathbf{p}_\ell) \geq \tau_{\text{full}}} \frac{s_{\ell,j}(\mathbf{h})}{S_\ell(\mathbf{h})} \geq \tau_{\text{frac}}\right]. \quad (17)$$

We report *Full fraction absorption* by averaging $\beta_\ell(\mathbf{h})$ over false negatives and then over eligible letters. We include a letter ℓ only if the ground-truth probe achieves $F1 \geq 0.6$, and we require at least 20 eligible letters.

F.2 Interpretability Experiments

F.2.1 Finding specific groups for Temporal and Geographical concepts

Automated group screening. To identify candidate groups, we rank all groups by how selectively their activations respond to a target concept (temporal or geographical) at the token level. We construct two evaluation sets, (i) a synthetic prompt suite with explicit concept terms, and (ii) a natural-text slice from OpenWebText to check that selectivity carries over to real contexts.

Prompt templates. For each concept family we define a lexicon of terms and instantiate sentence templates by substituting {term}. We generate all term-template combinations, shuffle, and keep at most `max_prompts=800` prompts per family.

Geography templates

I traveled to {term}.
She moved to {term} for work.
He lives in {term} now.
The city of {term} is famous.
The region around {term} is beautiful.
We drove across {term}.
The capital of {term} is well known.
The border of {term} is disputed.
Flights to {term} were delayed.
A map of {term} was published.
The river in {term} floods in spring.
The cuisine of {term} is popular.
{term} appears on the map.
The mountains in {term} are high.
The coastline of {term} is long.
The embassy in {term} reopened.

Temporal templates

The event happened in {term}.
The meeting is on {term}.
She will return in {term}.
They met every {term}.
He works best in the {term}.
The deadline is {term}.
We arrived {term}.
The festival is held in {term}.
The schedule changed by {term}.
She called me on {term}.
The report is due in {term}.
The appointment is {term}.
He studies each {term}.
We meet once a {term}.
The contract ends in {term}.
The anniversary is in {term}.

Negative templates

I bought a {term} at the store.
She found a {term} in the garden.
He repaired the {term} at home.
We cooked a {term} for dinner.
The {term} was on the table.
A {term} fell from the shelf.
He cleaned the {term} yesterday.
She carried a {term} to work.
The {term} needs a new battery.
They painted the {term} blue.

Token-level activations and labels. For each prompt, we run a forward pass, cache the residual stream at the SAE hook, and compute encoder activations. We reshape the SAE activations into group coordinates $a_{t,g} \in \mathbb{R}^r$ for each token position t and group g , and use the group norm $\|a_{t,g}\|_2$ as the scalar activation for selectivity scoring. Tokens are labeled positive if their normalized string matches the corresponding lexicon. For temporal concepts, we additionally label any token matching a four-digit year pattern as positive.

Ranking metrics and hyperparameters. For each group we compute AUC between positive and negative tokens using $\|a_{t,g}\|_2$, Cohen’s d based on the difference in means, and precision at

an “active” threshold defined per-group as the `quantile=0.99` quantile of $\|a_{t,g}\|_2$. We use `seed=42` and `batch_size=16`. We also rerun the same token-level evaluation on an OpenWebText slice (`corpus_docs=200`, `corpus_max_tokens=128`, stopping once at least `corpus_min_pos=200` positive tokens are observed). As a sanity check, we fit an ℓ_1 -regularized logistic-regression probe on the full vector of group norms per token and inspect the largest positive weights.

Selection. For geography, the analysis of Mistral SASA consistently identifies Group 1570 as a strong, robust geography-selective group with $\text{AUC} = 0.98$, Cohen’s $d = 4.36$, and ℓ_1 -LR weight = 0.99, and we use it in the downstream analysis. For temporal concepts, we select Group 1473 similarly with $\text{AUC} = 0.94$, Cohen’s $d = 2.42$, and ℓ_1 -LR weight = 0.96.

F.2.2 Token Activation Profiles

A token activation profile visualizes where a group fires within a prompt. Given a prompt, we compute $\|a_{t,g}\|_2$ for each token position t and plot this value as a function of token index.

Temporal prompts and hyperparameters. For Group 1473 we use three fixed prompts containing days, months, years, and seasons.

On Monday, March 3, 1997, the committee met in private session.
 On Friday, September 21, 2001, the city was marked by heavy rain.
 In the summer of 2012, the team traveled to Europe for training.

Geography prompts and hyperparameters. For Mistral SASA Group 1570 we use three fixed prompts spanning city, country, and continent mentions.

A storm delayed my flight to Chicago in the US.
 The Toronto skyline in Canada is impressive.
 Our team met in Paris in France before heading back from Europe.

OpenWebText activation examples. Furthermore, Table 4 lists five OpenWebText contexts with the highest Group 1473 activations (group norms), highlighting the most active token.

Activation	Prompt
14.936	Attorney General Dominic Grieve was presented with legal papers on Monday arguing that because there were no fingerprints on five items found with
14.880	state of Chihuahua returned to the United States on Friday night. The four-year-old remained in the custody
14.703	office. The draft resolution, circulated by Egypt on Wednesday night and originally slated for a vote Thursday, demands
14.602	President Trump made his debut at the United Nations on Tuesday , addressing the U.N. General Assembly at its annual
14.506	s president Uhuru Kenyatta said in a speech on Tuesday (Feb. 16) that his government is thinking about building

Table 4: Activation values and corresponding OpenWebText prompts for GPT-2 SASA Group 1473.

F.2.3 Structure of subspaces

What the points represent. For a fixed group g , each point in a geometry plot corresponds to the group coordinate vector $a_{t,g} \in \mathbb{R}^r$ at a token position t where the token matches a concept instance (for example, a month name or a city name). We then project these vectors with PCA for visualization.

Temporal subspace (Group 1473). We construct a set of target tokens for days of the week, months, seasons, and years in the range 1980–2024, including their abbreviations, retaining only single-token terms under the model tokenizer. We stream OpenWebText, process 2000 documents truncated to 128 tokens, and collect at most 40 vectors per label. To focus on confident activations, we retain occurrences with group norm above 0.1. We standardize all collected vectors and fit PCA. The plotted points are the PCA-projected group coordinates, colored by temporal category.

Geographical subspace (Mistral SASA Group 1570). We use the RAVEL city dataset, which comprises 3552 cities, along with their associated countries and continents. For each city, we form an evaluation prompt of the form `City: {city}. Country: {country}. Continent: {continent}.` and run the model with padding and truncation to 96 tokens. We locate the token spans corresponding to the city, country, and continent strings. If an entity spans multiple tokens, we average $a_{t,g}$ across the span. We then average across all prompts to obtain a single vector for each city and each country, standardize the combined set, and fit a 2D PCA for the scatter plot (subsampling cities to at most 2000 points for readability).

F.2.4 Temporal Concept cyclic season recovery

Month centroids. Using the same OpenWebText collection described above, we take all vectors labeled as months and compute a centroid vector for each month name by averaging its collected group coordinates.

Circular projection. To test whether the learned representation respects the cyclic calendar topology, we fit a linear map from group space to \mathbb{R}^2 that sends month centroids to evenly spaced points on the unit circle in chronological order. Concretely, for month index $m \in \{1, \dots, 12\}$ we set the target to $(\cos(2\pi m/12), \sin(2\pi m/12))$ and solve a ridge-regularized least-squares problem with ridge coefficient 10^{-6} .

Season ordering plot. We apply this projection to the month centroids, compute season centroids by averaging projected months within each season (Winter is Dec–Feb, Spring is Mar–May, Summer is Jun–Aug, Autumn is Sep–Nov), and plot both months and seasons in the learned 2D coordinates. The resulting figure visualizes whether the four seasons appear in the expected cyclic order.

G Feature Analysis: Geographical Concepts

Analogous to temporal concepts, geographical knowledge in LLMs is also inherently structured. We identify that Mistral-7B SASA learns a coherent *Geographical Subspace* (Mistral SASA Group 1570) that unifies the concepts of city, country, and continent. As shown in the activation profiles in Figure 8, this group activates robustly across distinct levels of granularity. It fires on cities (“Chicago”, “Paris”), countries (“US”, “France”), and continents (“Europe”) within natural contexts. The PCA visualization in Figure 9 demonstrates that the subspace organizes these entities into distinct, geometrically related clusters.

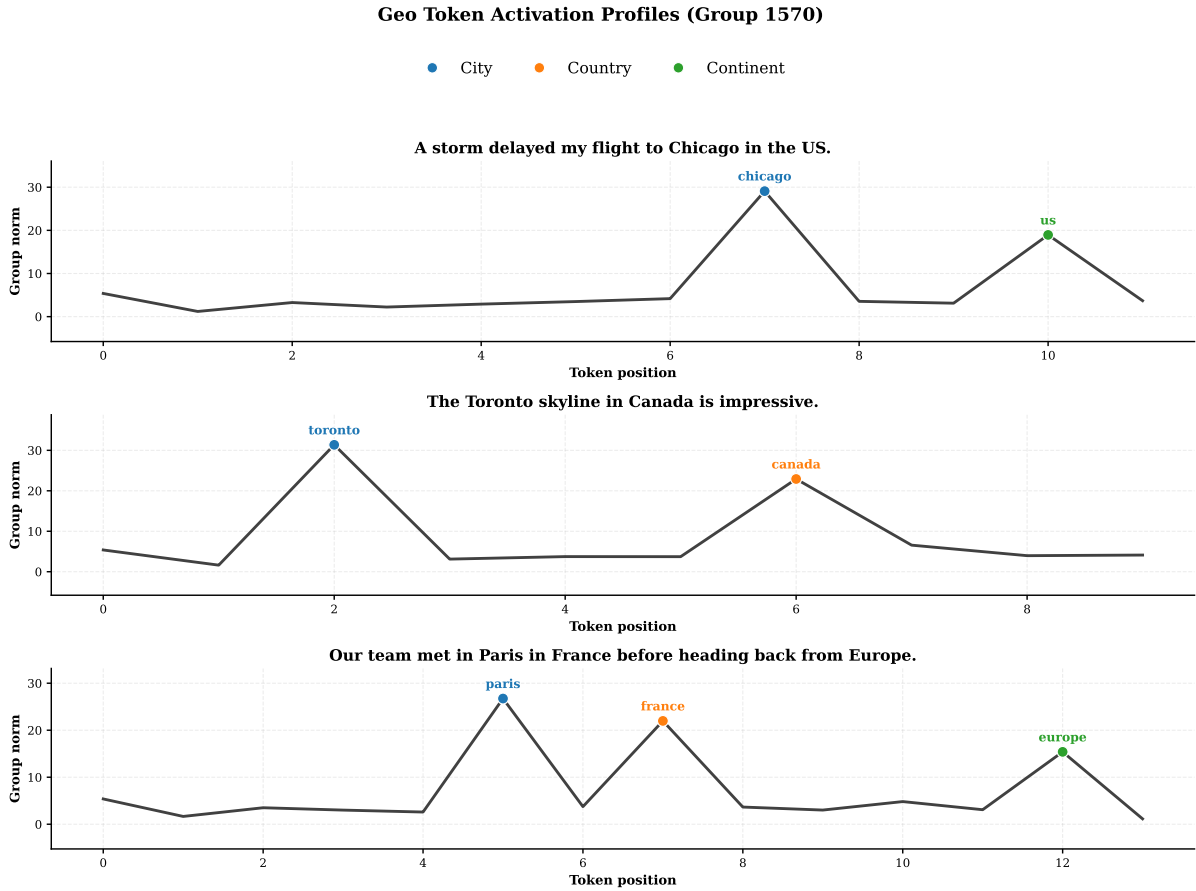


Figure 8: **Mistral SASA Group 1570 Activation Profiles.** The group consistently activates on geographical tokens.

H Feature analysis: Sports Concepts

SASA’s subspaces extend beyond temporal and geographical concepts. Figure 10 shows Group 1056, which AutoInterp labels as *Sports and athletic activity terms* with score 1.0. Within this subspace, 3D PCA separates combat/action terms (fight, round, boxing), titles/achievement terms (champion, championship, tournament), and general sports context into three geometrically distinct families.

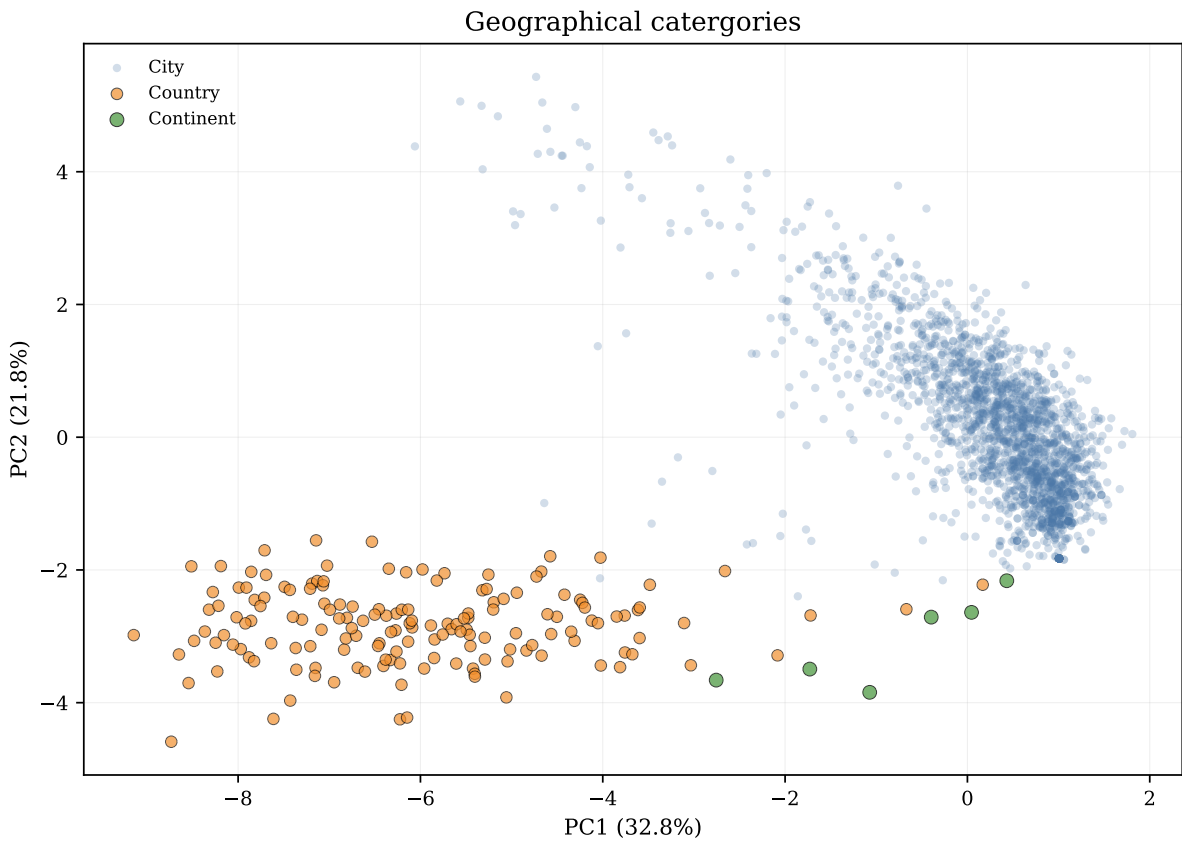


Figure 9: **Geometry of the Geographical Subspace.** A PCA projection of the latent activations in Mistral SASA Group 1570. The subspace organizes geographical concepts into distinct clusters, preserving the hierarchical distinction between cities (blue), countries (orange), and continents (green).

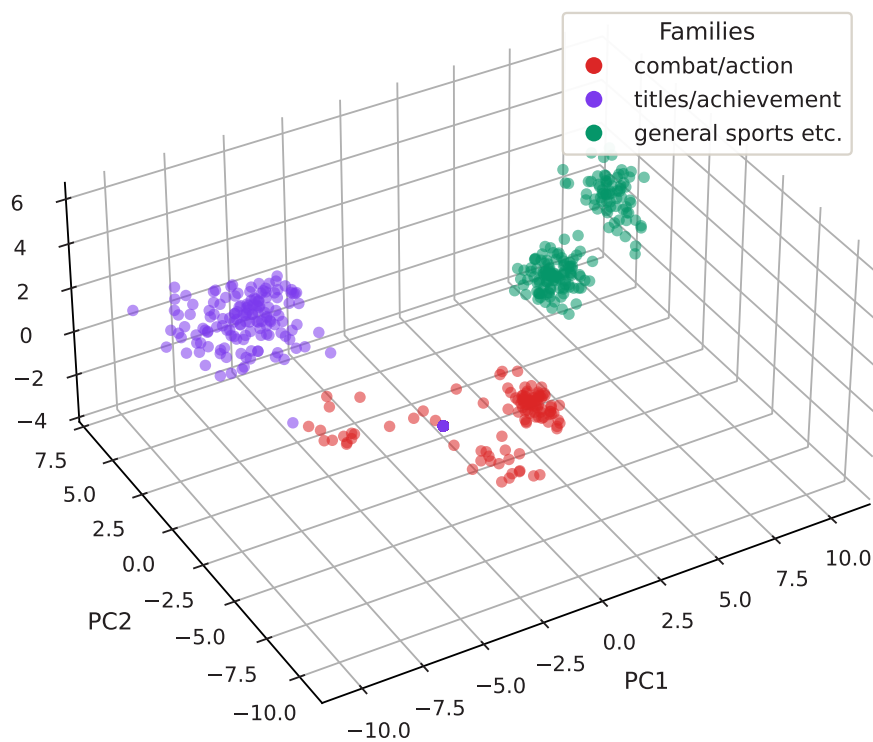


Figure 10: **SASA Group 1056 — Sports subspace.** AutoInterp labels this group as *Sports and athletic activity terms*. A 3D PCA view separates combat/action, titles/achievement, and general sports contexts (e.g., sport, athletic).